

1

# Snow Interception Relationships with 2 Meteorology and Canopy Structure in a 3 Subalpine Forest

4

5 **Authors:**

6 A. Cebulski<sup>1</sup> (ORCID ID - 0000-0001-7910-5056)

7 J.W. Pomeroy<sup>1</sup> (ORCID ID - 0000-0002-4782-7457)

8 <sup>1</sup>Centre for Hydrology, University of Saskatchewan, Canmore, Canada

9 **Corresponding Author:** A. Cebulski, alexcebulski@gmail.com

10 **Abstract:** Snow accumulation models differ in how snow interception and ablation processes  
11 are represented and thus their application to diverse climates and forest types is uncertain.  
12 Existing parameterizations of initial snow interception before unloading include inherently  
13 coupled canopy snow accumulation and ablation processes. This leads to difficulty in di-  
14 agnosing processes and adding possible errors to simulations when incorporated as canopy  
15 interception routines in models that already account for canopy snow ablation. This study  
16 evaluates the theory underpinning parameterizations of initial snow interception using high-  
17 temporal resolution and fine-scale measurements of throughfall for events with minimal snow  
18 ablation and redistribution in both the canopy and on the ground. The relationship between  
19 these throughfall measurements, event meteorology, and a novel lidar-based canopy structure  
20 measurement are assessed in two subalpine forest plots in the Canadian Rockies. Contrary  
21 to existing theories, no association of canopy snow load or air temperature with interception

efficiency was observed. Instead, canopy structure emerged as the primary factor governing snow accumulation. A wind-driven snowfall event demonstrated that non-vertical hydrometeor trajectories can significantly increase snow-leaf contact area, thereby enhancing initial interception before ablation. Prediction of interception efficiency for this event improved dramatically when adjusted for hydrometeor trajectory angle based on a wind speed at one-third of the canopy height. Snow-leaf contact area showed a high sensitivity to wind speed, increasing by up to 95% with a  $1 \text{ m s}^{-1}$  wind speed. The study proposes a new parameterization that calculates throughfall, independent of processes that ablate snow from the canopy, as a function of snow-leaf contact area adjusted for hydrometeor trajectory angle. This new parameterization successfully estimated subcanopy snow accumulation for a snowfall event at two forest plots measured using lidar and snow surveys. By separating canopy snow ablation from snow interception processes, this new model offers potentially improved prediction of subcanopy snow accumulation when combined with canopy snow ablation parameterizations.

**Keywords:** snow interception, throughfall, ablation, forest, snowpack, lidar, process-based modelling

## 1 Introduction

Over half of North America's snow-covered zone is covered by forests (Kim et al., 2017), significantly impacting the accumulation and redistribution of snowpacks and subsequent snowmelt runoff. Essery et al. (2003) estimated that 25–45% of annual snowfall may be lost to the atmosphere due to sublimation of snow intercepted in forest canopies globally. Snow intercepted in the canopy can sublimate and melt at much higher rates than the subcanopy snowpack (Katsushima et al., 2023; Lundberg & Halladin, 1994; Pomeroy et al., 1998), reducing the amount of snow available for runoff. Vegetation structure is one of the primary factors controlling the partitioning of snowfall into throughfall and interception (Hedstrom & Pomeroy, 1998; Storck et al., 2002), and thus governs the quantity of snow subject to sublimation from the canopy. However, forest thinning efforts aimed at limiting sublimation losses to increase

48 snowmelt runoff do not always lead to a corresponding increase in spring streamflow (Golding  
49 & Swanson, 1978; Harpold et al., 2020; Pomeroy et al., 2012; Troendle, 1983). This may be  
50 due to increased ablation rates when forest cover is reduced, desynchronization of snowmelt,  
51 and sub-surface hydrology interactions (Ellis et al., 2013; Musselman et al., 2015; Pomeroy et  
52 al., 1997; Safa et al., 2021; Varhola et al., 2010). Given the significant impact of forest cover  
53 on snowpacks, along with the limited or absent monitoring networks for subcanopy snow accu-  
54 mulation (Rittger et al., 2020; Vionnet et al., 2021), land management, ecological conservation,  
55 and water resource decisions depend on reliable models of snow redistribution.

56 Hedstrom & Pomeroy (1998), working in the cold continental boreal forest, proposed that  
57 initial snow interception efficiency was controlled by the maximum canopy load which itself  
58 was a function of leaf area index and new snow density. Unloading was found to be an expo-  
59 nential function of time and observed only days or weeks after the interception event. Storck  
60 et al. (2002), working in temperate coastal forests, emphasized the role of leaf area index  
61 and air temperature in controlling the maximum canopy snow load. Gelfan et al. (2004)  
62 demonstrated accurate subcanopy snowpack simulations at study sites in Russia by treating  
63 the Hedstrom & Pomeroy (1998) and Storck et al. (2002) parameterizations separately while  
64 using a step-based function to choose either parameterization based on air temperature. A  
65 similar parameterization in the Cold Regions Hydrological Model (Pomeroy et al., 2022) has  
66 shown strong performance at sites across Canada, northern United States, Switzerland, and  
67 Spain. However, overestimation of subcanopy snow accumulation was reported by Lundquist  
68 et al. (2021) and Lumbrazo et al. (2022) when combining the Hedstrom & Pomeroy (1998)  
69 routine with ablation parameterizations from different studies (e.g., Roesch et al., 2001). The  
70 coupling of ablation processes within existing snow interception models (Hedstrom & Pomeroy,  
71 1998; Storck et al., 2002) may contribute to overestimates of throughfall, canopy snow unload-  
72 ing, and canopy snow melt when combined with other canopy snow ablation parameterizations  
73 (Cebulski & Pomeroy, 2024). Additional observations of snow interception that exclude abla-  
74 tion processes could help determine the applicability of the interception theories proposed by  
75 Hedstrom & Pomeroy (1998) and Storck et al. (2002). Hedstrom & Pomeroy's (1998) theory

76 also suggests that moderate wind speeds, which can result in more horizontal hydrometeor tra-  
77 jectories, increasing snow-leaf contact area and interception efficiency at the plot scale. This  
78 association has also been shown in rainfall interception studies to decrease throughfall of rain  
79 (Herwitz & Slye, 1995; Van Stan et al., 2011). However, the relationship proposed by Hed-  
80 strom & Pomeroy (1998), is typically not included in snow accumulation models as empirical  
81 testing of this relationship is lacking.

82 The objective of this paper is to evaluate the theories underlying existing snow interception  
83 models using high spatial and temporal resolution measurements of subcanopy snow accumu-  
84 lation for events with minimal canopy snow ablation. These new observations are investigated  
85 to address the following research questions:

- 86 1. Are the existing theories regarding the relationships between meteorology and forest  
87 structure and initial snow interception supported by in-situ observations?
- 88 2. Is snow interception influenced by non-vertical hydrometeor trajectory angles over a  
89 wind-driven snowfall event?
- 90 3. To what extent can these findings inform the development of a new parameterization for  
91 snow interception?

## 92 **2 Theory**

### 93 **2.1 Snow interception**

94 The change in canopy snow load over time,  $\frac{dL}{dt}$  ( $\text{kg m}^{-2} \text{ s}^{-1}$ ), can be estimated from the mass  
95 balance:

$$\frac{dL}{dt} = q_{sf} + q_{ros} - q_{tf} - q_{unld} - q_{drip} - q_{wind}^{veg} - q_{sub}^{veg} \quad (1)$$

where  $q_{sf}$  is the snowfall rate ( $\text{kg m}^{-2} \text{ s}^{-1}$ ),  $q_{ros}$  ( $\text{kg m}^{-2} \text{ s}^{-1}$ ) is the rate of rainfall falling on snow intercepted in the canopy,  $q_{tf}$  ( $\text{kg m}^{-2} \text{ s}^{-1}$ ) is the throughfall rate ( $\text{kg m}^{-2} \text{ s}^{-1}$ ),  $q_{unld}$  is the canopy snow unloading rate ( $\text{kg m}^{-2} \text{ s}^{-1}$ ),  $q_{drip}$  is the canopy snow drip rate due to canopy snowmelt ( $\text{kg m}^{-2} \text{ s}^{-1}$ ),  $q_{wind}^{veg}$  is the wind transport rate in or out of the control volume ( $\text{kg m}^{-2} \text{ s}^{-1}$ ), and  $q_{sub}^{veg}$  is the intercepted snow sublimation rate ( $\text{kg m}^{-2} \text{ s}^{-1}$ ). During periods with low air temperatures and low wind speeds,  $q_{ros}$ ,  $q_{unld}$ ,  $q_{drip}$ ,  $q_{wind}^{veg}$ , and  $q_{sub}^{veg}$  can be assumed negligible. Figure 1 in Cebulski & Pomeroy (2024) presents a visual representation of this mass balance.

Interception efficiency,  $\frac{I}{P}$  (-), which is the fraction of snowfall intercepted over  $\Delta t$  before ablation, can be calculated as:

$$\frac{I}{P} = \frac{\Delta L}{q_{sf}\Delta t} \quad (2)$$

and throughfall,  $q_{tf}$  can be calculated as:

$$q_{tf} = \left(1 - \frac{I}{P}\right) \cdot q_{sf} \quad (3)$$

## 2.2 Hydrometeor trajectory angle

Herwitz & Slye (1995) calculate the trajectory angle of a hydrometeor,  $\theta_h$ , as the departure in degrees ( $^\circ$ ) from a vertical plane as:

$$\theta_h = \arctan\left(\frac{x_h(u_z)}{v_h(D_h)}\right) * \frac{180}{\pi} \quad (4)$$

where  $v_h(D_h)$  is the terminal fall velocity of the hydrometeor ( $\text{m s}^{-1}$ ), which is a function of the hydrometeor diameter,  $D_h$  and  $x_h(u_z)$  is the horizontal velocity of the hydrometeor ( $\text{m s}^{-1}$ ) which is a function of the within canopy wind speed,  $u_z$  at height above ground,  $z$ . This assumes the hydrometeors are following fluid points in the atmosphere.

<sup>114</sup> **3 Data and methods**

<sup>115</sup> **3.1 Study site**

<sup>116</sup> This study was conducted at Fortress Mountain Research Basin (FMRB), Alberta, Canada,  
<sup>117</sup> -115° W, 51° N, a continental headwater basin in the Canadian Rockies (Figure 1). Data from  
<sup>118</sup> this study was collected between October 2021 and July 2023 within and surrounding two  
<sup>119</sup> forest plots adjacent to the FMRB Powerline Station (PWL) and Forest Tower Station (FT)  
<sup>120</sup> at ~2100 m above sea level as shown in Figure 1. The average annual precipitation at PWL  
<sup>121</sup> Station from 2013 to 2023 was 1045 mm, with the peak annual snow water equivalent (SWE)  
<sup>122</sup> reaching 465 kg m<sup>-2</sup>, typically occurring in late April. The PWL and FT forest plots include  
<sup>123</sup> discontinuous stands of 70% subalpine fir (*Abies lasiocarpa*) and 30% Engelmann spruce (*Picea*  
<sup>124</sup> *engelmannii*) (Langs et al., 2020). The PWL plot is located 120 m to the northwest of FT  
<sup>125</sup> station and contains a forest clearing with a diameter of ~12 m, surrounded by a closed canopy.  
<sup>126</sup> The FT plot has a discontinuous canopy without artificial clearings. The canopy coverages of  
<sup>127</sup> the two forest plots are 0.51 and 0.29 and the winter leaf area indices are 2.07 and 1.66 for  
<sup>128</sup> PWL and FT respectively. The average height of the canopy surrounding the plot to the east  
<sup>129</sup> of the PWL station is 10.5 m and surrounding the forest plot around the FT Station is 7.1  
<sup>130</sup> m. In August of 1936, the majority of vegetation in FMRB burned during a large forest fire  
<sup>131</sup> that affected most of the Kananaskis Valley (Fryer et al., 1988). Following the fire, the forest  
<sup>132</sup> within the PWL and FT forest plots has naturally regenerated, though some trees have been  
<sup>133</sup> removed for road clearing and creation of a snow study plot.

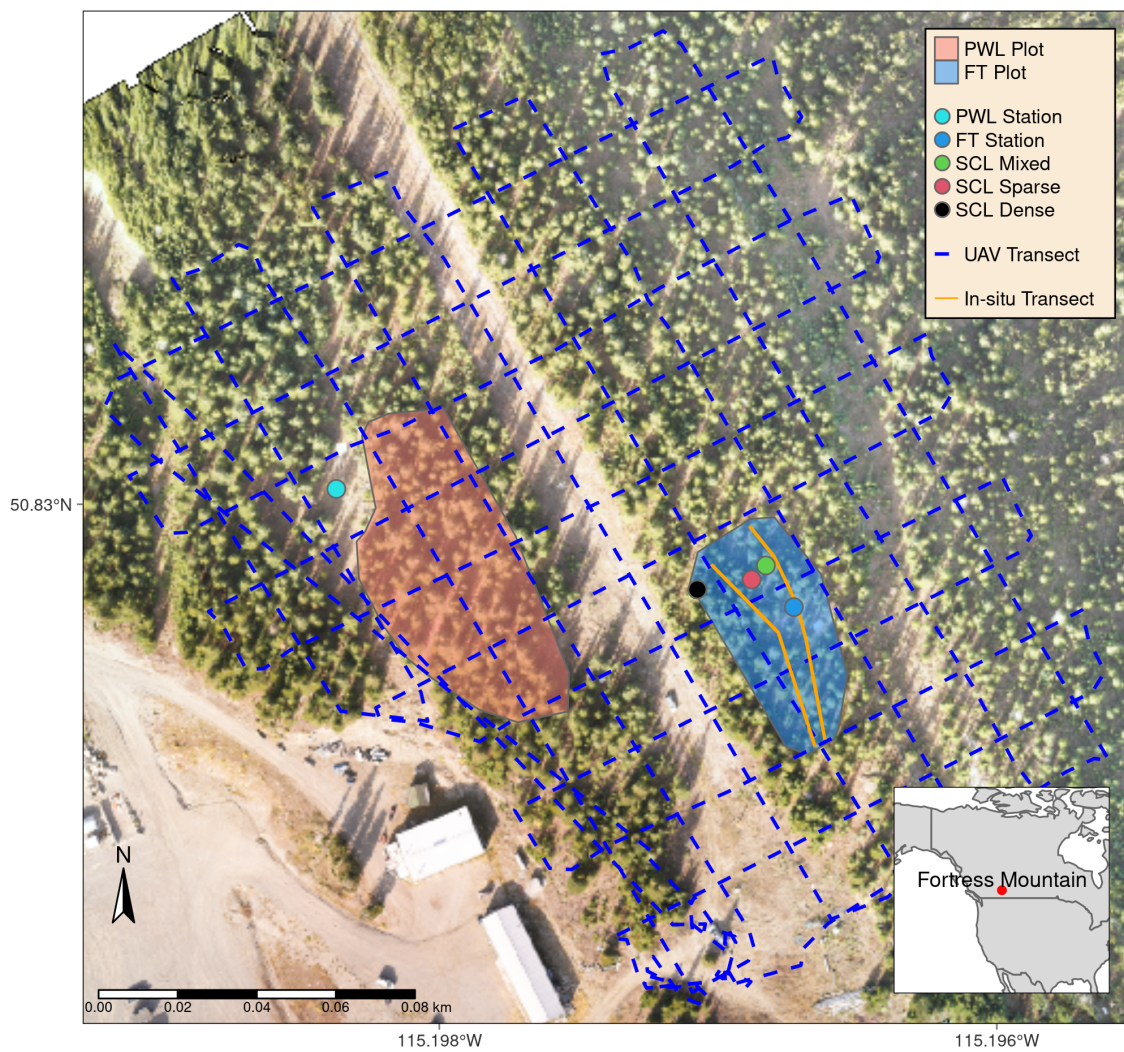


Figure 1: Map showing the location of forest plots, flux towers, subcanopy lysimeter instruments (SCL), and survey transects. The inset map on the lower right shows the regional location of Fortress Mountain Research basin.

<sup>134</sup> **3.2 Meteorological measurements**

<sup>135</sup> Measurements of air temperature and relative humidity (Vaisala model HMP155A), wind speed  
<sup>136</sup> and direction (RM Young model 86000 2-D ultrasonic anemometer) were made 4.3 m above the  
<sup>137</sup> ground at FT station (Figure 1). Wind speed measurements from a 3-cup anemometer (Met  
<sup>138</sup> One model 014A), installed adjacent to the 2-D ultrasonic anemometer at 4.3 m, were used for  
<sup>139</sup> gap filling wind speed. Additional wind speed measurements were collected by two 3D sonic  
<sup>140</sup> anemometers (Campbell Scientific CSAT3) installed at 2 m (raised to 3 m February 2022) and  
<sup>141</sup> 13.5 m above the ground at FT station. Average wind speeds at these three heights were found  
<sup>142</sup> to follow a logarithmic relationship. Thus, a wind profile was fitted to these measurements  
<sup>143</sup> using the Prandtl-von Kármán log-linear relationship:

$$\bar{u} = \frac{u_*}{k} \ln\left(\frac{z - d_0}{z_0}\right) \quad (5)$$

<sup>144</sup> where  $\bar{u}$  is average wind speed ( $\text{m s}^{-1}$ ) at height,  $z$  (m) above the ground,  $u_*$  is the friction  
<sup>145</sup> velocity ( $\text{m s}^{-1}$ ),  $d_0$  is the displacement height (m),  $z_0$  is the roughness length of momentum  
<sup>146</sup> (m), and  $k$  is the dimensionless von Kármán Constant (0.4).

<sup>147</sup> Using wind speed measurements at three heights at FT station, collected during events when  
<sup>148</sup> the instruments were confirmed to be free of snow, the function ‘optim’ from the ‘stats’ R  
<sup>149</sup> package (R Core Team, 2024) was used to estimate the values  $d_0$  and  $z_0$  for Equation 5 that  
<sup>150</sup> best fit the observed mean wind speed. The parameters found for the wind speed profile  
<sup>151</sup> include a  $d_0$  of 0.58 m and  $z_0$  of 0.50 m. See the supporting information for more information  
<sup>152</sup> on the development and testing of the wind profile.

<sup>153</sup> At PWL station, the snowfall rate was measured by an Alter-shielded OTT Pluvio weighing  
<sup>154</sup> precipitation gauge 2.6 m above ground, corrected for undercatch following phase correction  
<sup>155</sup> by Harder & Pomeroy (2013) and catch efficiency by Smith (2007). Wind speed for undercatch  
<sup>156</sup> correction was measured by a 3-cup anemometer (Met One model 014A) at a height of 2.6 m at  
<sup>157</sup> PWL station. An optical disdrometer (OTT Parsivel2) provided measurements of hydrometeor

158 particle size and vertical velocity. All measurements were recorded at 15-min intervals using  
159 Campbell Scientific dataloggers, except the Parsivel2 which was recorded at 1-minute intervals  
160 by an onsite computer.

161 **3.3 Lysimeter measurements**

162 Three subcanopy lysimeters (SCLs) were installed surrounding the FT Station (Figure 1) to  
163 provide 15-minute interval measurements of throughfall as in MacDonald (2010). Figure 2  
164 shows the three SCLs which consisted of a plastic horse-watering trough with an opening of  
165 0.9 m<sup>2</sup> and depth of 20 cm suspended from a load cell (Intertechnology 9363-D3-75-20T1)  
166 attached to an aluminum pipe connected between two trees. For 26 distinct snowfall events,  
167 where canopy snow ablation rates were deemed negligible, snow captured in the SCLs was  
168 assumed to be throughfall. The throughfall rate,  $q_{tf}$ , was calculated by dividing the weight  
169 of snow in the SCL by the cross-sectional area of the SCL opening and determining the rate  
170 of change at 15-minute intervals. Canopy snow load was estimated at the same 15-minute  
171 intervals during these events using Equation 1 and incorporating measurements of  $q_{tf}$  from  
172 the SCLs and  $q_{sf}$  from the PWL snowfall gauge. Rates of  $q_{ros}$ ,  $q_{unld}$ ,  $q_{drip}$ ,  $q_{wind}^{veg}$ , and  $q_{sub}^{veg}$   
173 were assumed to be zero for these periods. Interception efficiency was also calculated for  
174 these intervals using Equation 2. Timelapse imagery, mass change on a weighed tree lysimeter  
175 “hanging tree” (Pomeroy & Schmidt, 1993) and in-situ observations were used to ensure the  
176 ablation of snow intercepted in the canopy was minimal over each interval. Additionally,  
177 the  $q_{tf}$  measurements were filtered to include observations with a snowfall rate  $> 0 \text{ kg m}^{-2}$   
178  $\text{hr}^{-1}$ , throughfall rate  $> 0.05 \text{ kg m}^{-2} \text{ hr}^{-1}$  and a snowfall rate greater than the SCL measured  
179 throughfall rate to minimize observations with unloading. The weighed tree lysimeter, a live  
180 subalpine fir (*Abies lasiocarpa*) tree suspended from a load cell (Artech S-Type 20210-100)  
181 measured the weight of canopy snow load (kg). This weight was scaled to an areal estimate of  
182 canopy snow load ( $L$ , kg m<sup>-2</sup>) using measurements of areal throughfall (kg m<sup>-2</sup>) from manual  
183 snow surveys and snowfall from the PWL Station snowfall gauge (see description of method  
184 in Pomeroy & Schmidt, 1993). The canopy structure surrounding three SCLs is shown in

<sup>185</sup> Figure 2 and was measured using hemispherical photography (Nikon Coolpix 4500 and EC-F8  
<sup>186</sup> hemispherical lens) and the hemispheR R package Chianucci & Macek (2023). The leaf area  
<sup>187</sup> index and canopy coverage from hemispherical photo analysis is shown in Table 1.

Table 1: Canopy structure of the three subcanopy lysimeters (SCL) located proximal to the FT Station. Leaf area index (LAI) and Canopy Coverage was measured using hemispherical photo analysis with the R package hemispheR.

Name	LAI (-)	Canopy Coverage (-)
Sparse	1.59	0.73
Mixed	1.86	0.78
Closed	2.11	0.82

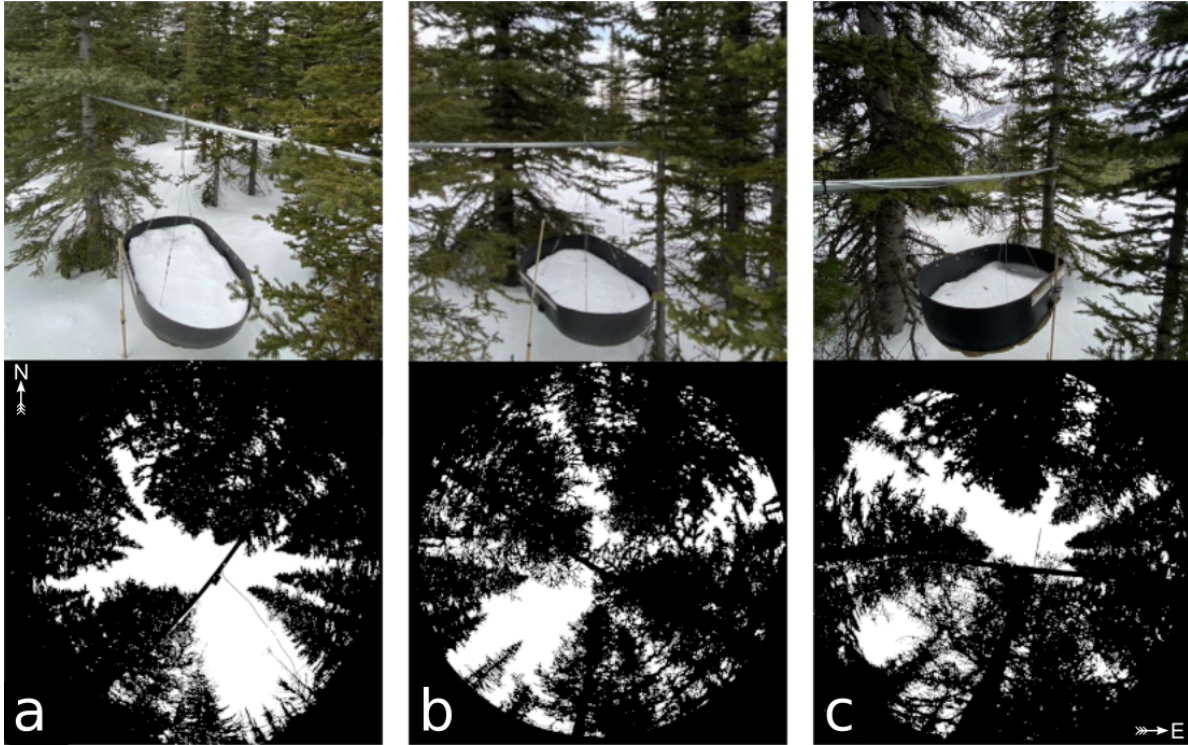


Figure 2: Images of the three subcanopy lysimeters (SCL) and surrounding canopy located in sparse (a), mixed (b), and dense (c) canopy. The top row presents a side view of each SCL and the bottom row shows hemispherical photographs classified using the hemispheR R package. These hemispherical images are oriented with north at the top and have been flipped to provide a view from above (i.e., east is on the right side of each image). See Table 1 for the canopy structure measurements of the canopy above each SCL.

### **188 3.4 UAV-Lidar data collection and processing**

189 The UAV (FreeFly Alta X) payload included a REIGL miniVUX-2 airborne laser scanner,  
 190 an Applanix APX-20 inertial measurement unit (IMU) and global navigation satellite system  
 191 (GNSS). The UAV was flown 90 m above the ground at a speed of  $3 \text{ m s}^{-1}$  following the  
 192 path shown in Figure 1. A detailed description of the UAV, payload, and flight settings is  
 193 provided in the supporting information. The methods outlined by Harder et al. (2020) and  
 194 Staines & Pomeroy (2023) were incorporated to reconcile survey lidar, IMU and GNSS data.

195 A systematic vertical bias of up to 6 cm between UAV-lidar flight lines was observed in the  
196 resulting point clouds on March 13<sup>th</sup> and 14<sup>th</sup>, 2024 and was attributed to IMU position  
197 drift. This offset between flight lines was corrected using the BayesStripAlign software v2.24  
198 (BayesMap Solutions, 2024). After strip alignment, the mean elevation bias in the point clouds  
199 was 0.000 m and the RMS error declined from 0.055 m to 0.038 m on March 13<sup>th</sup> and changed  
200 from 0.033 m to 0.029 m on March 14<sup>th</sup>. The point cloud density ranged from ~1200 returns m<sup>2</sup>  
201 in sparse forest to ~2200 returns m<sup>2</sup> in open clearings. Quality control, ground classification,  
202 calculation of surface elevation change (subtraction of the two UAV-lidar point clouds), and  
203 generation of 0.05 m resolution rasters was conducted using the LAStools software package  
204 (LAStools, 2024). Post processing and resampling of raster data to a 0.25 m grid cell resolution  
205 was conducted using the ‘Terra’ R package (Hijmans, 2024). More details on the UAV-lidar  
206 processing workflow are provided in the supporting information.

### 207 3.5 Snow surveys

#### 208 3.5.1 In-situ snow depth and density

209 Twelve in-situ fresh snow surveys (six pre- and post-snowfall event pairs) provided measure-  
210 ments of subcanopy throughfall depth and density at 30 locations following the transects shown  
211 in Figure 1 to upscale the weighed tree snow load from kg to kg m<sup>-2</sup> as in Pomeroy & Schmidt  
212 (1993). Minimal ablation and redistribution of snow was observed between the pre- and post-  
213 snowfall surveys. When conditions allowed for a UAV-lidar flight, the in-situ snow surveys  
214 were conducted following the UAV-lidar flight to assess the accuracy of the throughfall mea-  
215 surements and provide a fresh snow density for the calculation of SWE (kg m<sup>-2</sup>). A 1000 cm<sup>3</sup>  
216 Perla snow density wedge sampler (RIP Cutter, [https://snowmetrics.com/shop/rip-1-cutter-](https://snowmetrics.com/shop/rip-1-cutter-1000-cc/)  
217 1000-cc/) was used to measure the density of the fresh snow layer,  $\rho_{tf}$  (kg m<sup>-3</sup>) from snow  
218 pits. Throughfall depth measurements,  $\Delta HS$  were converted to SWE using the following  
219 equation:

$$\Delta SWE_{tf} = \Delta HS \cdot \overline{\rho_{tf}} \quad (6)$$

220 Differential GNSS rover coordinates, with  $\pm 2.5$  cm 3D uncertainty, were taken at each snow  
221 sampling location so the locations could be queried later from the UAV-lidar rasters to assess  
222 measurement error and were also used as input for the UAV-lidar strip alignment. If a pre-  
223 event crust layer was present, the depth of post event fresh snow accumulation above the crust  
224 layer was interpreted as throughfall over the event. In the absence of a defined crust layer, the  
225 difference in pre- and post-event snow depth to ground was interpreted as event throughfall.

226 **3.5.2 UAV-Lidar snow depth**

227 Two uncrewed aerial vehicle (UAV) lidar surveys were conducted before and after a 24-hour  
228 snowfall event that occurred between March 13<sup>th</sup> and March 14<sup>th</sup>, 2023 to facilitate the mea-  
229 surement of snow accumulation and canopy structure within the FT and PWL forest plots.  
230 This period was selected based on two criteria: 1) it provided sufficient cumulative snowfall  
231 to result in a low relative error in UAV-lidar measured throughfall, and 2) minimal snow  
232 redistribution and ablation was observed, as confirmed by the SCLs, weighed tree, and time-  
233 lapse imagery. The change in surface elevation between the two UAV-lidar point clouds was  
234 interpreted as the increase in snow accumulation,  $\Delta HS$  over the snowfall event.

235 **3.6 UAV-Lidar canopy metrics**

236 The canopy structure in the two UAV-lidar point clouds (March 13<sup>th</sup> and March 14<sup>th</sup>) was  
237 characterized using the voxel ray sampling (VoxRS) methodology for lidar data analysis, as  
238 developed by Staines & Pomeroy (2023). This method was chosen for its ability to provide  
239 canopy metrics that are less sensitive to the inherent non-uniform nature of lidar sampling data,  
240 which often results from beam occlusion in vegetation and leads to reduced points near the  
241 ground. Using this method radiation transmittance,  $\tau (-)$ , was measured across the hemisphere

242 at a  $1^\circ$  step, i.e., azimuth angles ( $0^\circ, 1^\circ, \dots, 359^\circ$ ) and zenith angles ( $0^\circ, 1^\circ, \dots, 90^\circ$ ) for each  
243  $0.25\text{ m}$  grid cell within the FT and PWL forest plots. The fraction of snow-leaf contact area  
244 per unit area of ground proposed by Hedstrom & Pomeroy (1998), and hereafter called leaf  
245 contact area ( $C_p$ ), was then calculated as:

$$C_p(C_c, \theta_h, L) = 1 - \tau \quad (7)$$

$$C_p(C_c, \theta_h, L) = \begin{cases} 1 - \tau, & \text{if } \theta_h > 0^\circ \\ 1 - \tau \approx C_c, & \theta_h = 0^\circ \end{cases} \quad (8)$$

246 where  $C_p$  is a function of the canopy coverage  $C_c$ ,  $\theta_h$  and  $L$ .  $C_p$  is approximately equal to  
247 canopy coverage ( $C_c$ ) for vertical snowfall trajectories.

248 **3.7 Statistics and regression models**

249 To determine how forest structure was associated with interception efficiency at different az-  
250 imuth and zenith angles over the March 13–14 snowfall event, the entire hemisphere at each  
251 grid location was considered. The relationship between interception efficiency and  $C_p$  was  
252 found to be linear and thus the Pearson Correlation Coefficient,  $\rho_p$  was calculated using the  
253 ‘stats’ package in R (R Core Team, 2024). The  $\rho_p$  was computed between a single raster of  
254 interception efficiency and each of the 32,760 rasters of  $C_p$ , representing locations across the  
255 hemisphere (azimuth [ $0^\circ, 1^\circ, \dots, 359^\circ$ ], zenith angle [ $0^\circ, 1^\circ, \dots, 90^\circ$ ]) at  $0.25\text{ m}$  grid cells spanning  
256 the FT and PWL forest plots.

257 Linear and non-linear regression models were developed to assess relationships in the observed  
258 data. Linear models were fitted using ordinary least squares regression via the ‘lm’ function  
259 from the R ‘stats’ package (R Core Team, 2024) to analyze two relationships: (1) between  
260 interception efficiency and meteorological variables and (2) between interception efficiency and  
261 leaf contact area. The latter was forced through the origin based on the theoretical justification

262 that the dependent variable should be zero when the independent variable is zero. Kozak &  
263 Kozak (1995) noted, the default  $R^2$  value provided for least squares models forced through the  
264 origin by many statistical packages can be misleading. Therefore, these  $R^2$  values were adjusted  
265 using Equation 10 in Kozak & Kozak (1995). Non-linear models were fitted to investigate the  
266 relationship of leaf contact area with simulated trajectory angle using non-linear least squares  
267 regression via the ‘nls’ function in ‘stats’ package in R.

## 268 **4 Results**

### 269 **4.1 The influence of meteorology on snow interception**

270 Canopy snow load was estimated for 26 snowfall events and increased linearly with cumulative  
271 event snowfall without evidence of reaching a maximum (Figure 3). Over these events, air  
272 temperature ranged from -24.5°C to 1°C, wind speeds at 4.3 m height ranged from calm to  
273 4.6 m s<sup>-1</sup> (Table 2), and wind direction was predominately from the southwest during snowfall  
274 (Figure 4). Missing canopy snow load measurements in Figure 3 for certain troughs during  
275 specific events was caused by damage to the subcanopy lysimeter wiring due to animals and  
276 heavy snow loads.

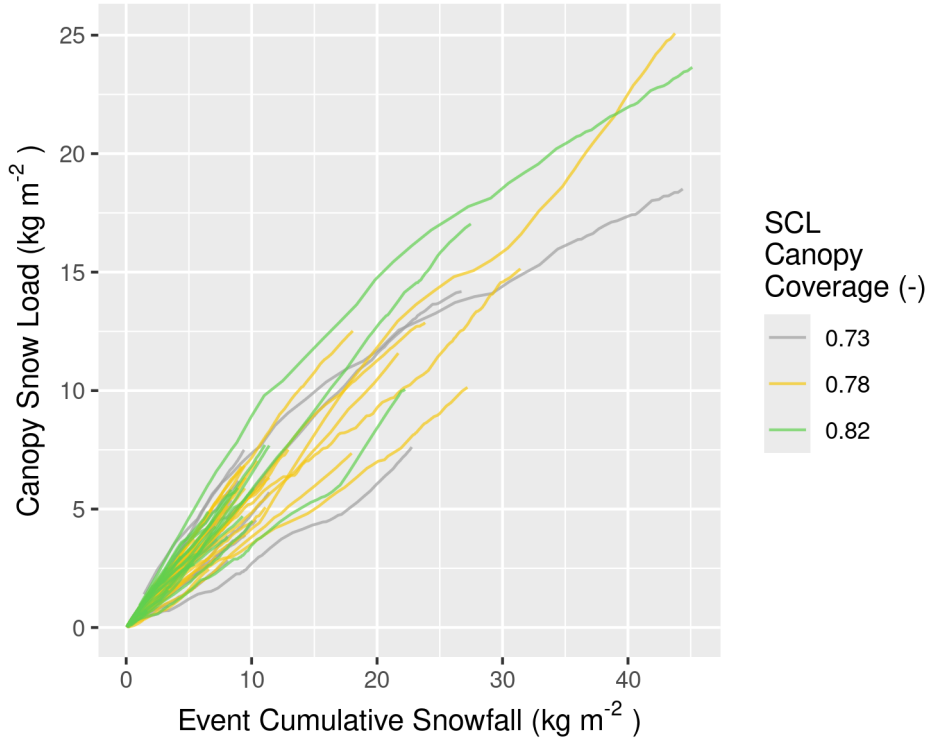


Figure 3: Plot showing the cumulative event snowfall versus the corresponding state of canopy snow load calculated using the subcanopy lysimeters (SCLs) for each of the 26 snowfall events. The SCLs are denoted by a distinct colour (grey, yellow, and green), correspond to varying canopy coverage (0.73, 0.78, and 0.82, respectively).

Table 2: Meteorology of the 26 snowfall events. Air temperature and wind speed were measured at FT station. Interception efficiency is estimated from snowfall measured at PWL station and the average throughfall of all three SCLs located within the FT forest plot (all from 15-min. measurements).

Start Date	Air Temperature (°C)			Wind Speed (m/s)			Interception Efficiency (-)			Snowfall (kg m <sup>-2</sup> )
	Min	Mean	Max	Min	Mean	Max	Min	Mean	Max	
2021-12-23	-6.2	-5.3	-4.6	0.6	3.1	4.6	0.7	0.8	1.0	21.7
2022-01-02	-15.9	-10.6	-5.8	0.2	1.9	4.2	0.1	0.7	1.0	32.9
2022-01-17	-14.8	-7.8	-0.8	0.2	1.1	1.8	0.0	0.6	1.0	12.9
2022-01-31	-24.5	-12.1	-6.4	0.1	1.0	1.7	0.2	0.7	1.0	9.1
2022-02-14	-9.9	-9.0	-8.5	0.4	0.8	1.2	0.2	0.5	0.8	1.7
2022-02-19	-4.7	-3.2	-2.5	1.3	2.3	3.6	0.3	0.6	0.9	11.1
2022-03-01	-8.3	-5.4	-1.0	0.1	1.0	3.1	0.4	0.8	1.0	9.9
2022-03-07	-12.5	-8.6	-4.4	0.3	0.8	1.7	0.3	0.7	1.0	9.5
2022-03-14	-2.7	-2.1	-0.8	1.0	1.6	2.9	0.2	0.6	0.9	8.4
2022-03-19	-3.1	-2.8	-2.5	0.0	0.7	1.3	0.3	0.5	0.6	6.6
2022-03-23	-7.9	-5.3	-0.9	0.8	1.2	1.8	0.4	0.6	0.9	1.6
2022-04-04	-3.5	-2.9	-2.1	0.6	1.0	1.9	0.0	0.4	0.6	3.4
2022-04-18	-5.2	-4.0	-2.7	0.4	1.1	1.9	0.1	0.5	0.9	7.4
2022-04-22	-2.8	-1.8	-0.5	0.4	0.8	1.2	0.1	0.5	1.0	9.8
2022-05-09	-4.9	-4.3	-3.2	0.1	0.4	0.9	0.2	0.5	0.9	8.1
2022-05-19	-4.9	-2.1	0.3	0.1	0.4	0.9	0.2	0.6	0.9	7.1
2022-06-13	-1.1	-0.3	0.6	0.1	0.1	0.4	0.0	0.5	0.9	45.3
2022-12-27	-3.0	-2.7	-1.9	0.6	1.1	1.8	0.2	0.5	0.9	4.5
2023-01-27	-11.5	-7.3	-4.5	0.6	0.9	1.2	0.1	0.5	0.8	10.4
2023-02-19	-14.3	-9.5	-6.3	0.2	0.8	1.4	0.2	0.7	1.0	18.1
2023-02-26	-9.2	-8.4	-6.6	0.2	1.0	2.1	0.3	0.5	1.0	5.4
2023-03-13	-8.9	-3.6	-0.1	0.3	1.3	2.2	0.0	0.5	1.0	27.4
2023-03-24	-7.9	-5.7	-3.5	0.1	0.5	1.2	0.1	0.4	0.7	23.8
2023-04-01	-8.9	-7.7	-4.7	0.1	0.6	1.4	0.4	0.6	0.8	11.4
2023-04-10	-1.1	-0.5	0.3	0.1	0.3	1.0	0.2	0.4	0.6	18.0
2023-05-08	0.2	0.6	1.0	0.4	0.6	0.8	0.6	0.6	0.7	3.5

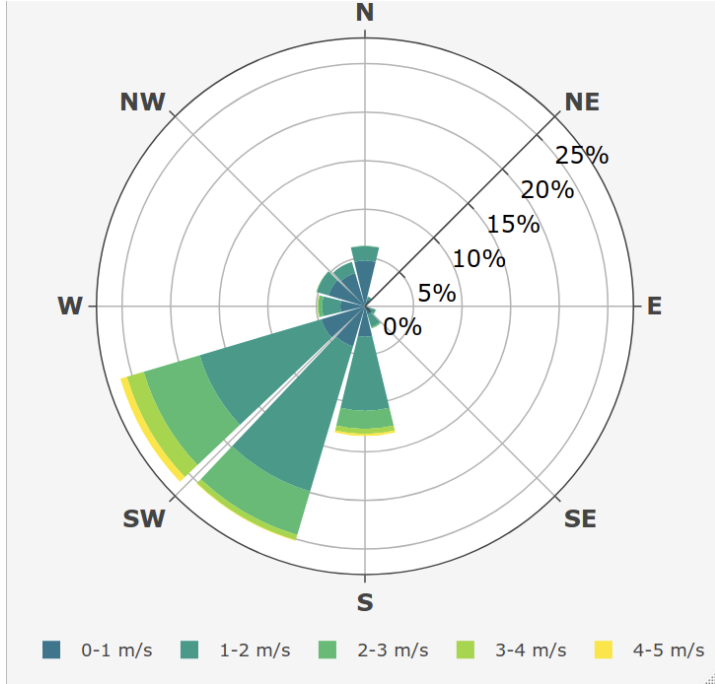


Figure 4: Wind rose showing the frequency of wind speed and direction over the 26 snowfall periods for the ultrasonic anemometer 4.3 m above ground at FT station.

Event average air temperature and interception efficiency were negatively associated for the mixed canopy ( $R^2 = 0.1$ ,  $p < 0.05$ ), but not associated at the closed and sparse canopies (Table 3 & Figure 5). Cumulative event snowfall was not associated with event interception efficiency at any site ( $p > 0.05$ ). Event wind speed was positively associated with interception efficiency for the sparse ( $R^2 = 0.1$ ,  $p > 0.05$ ) and closed ( $R^2 = 0.2$ ,  $p < 0.05$ ) canopies, both with limited canopy openings (Figure 2a,c) towards the prevailing wind direction shown in the wind rose in Figure 4. However, interception efficiency in the mixed canopy, which is partially open towards the prevailing wind direction, was not associated with wind speed ( $p > 0.05$ ).

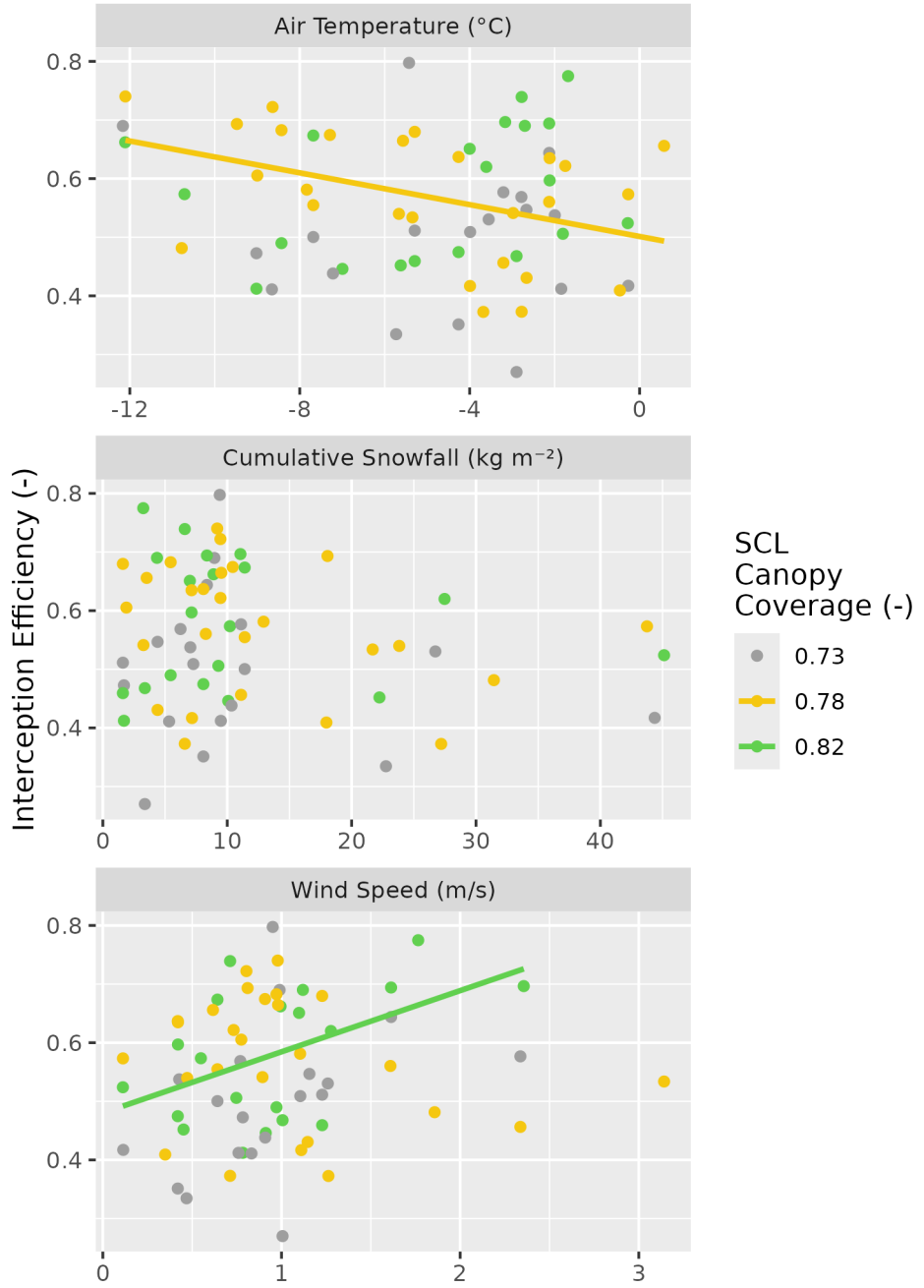


Figure 5: Scatter plots showing the event mean air temperature, mean wind speed, and cumulative snowfall versus the event mean interception efficiency estimated using the SCLs for each of the 26 snowfall events. The colours (grey, yellow, and green), correspond to varying canopy coverage (0.73, 0.78, and 0.82, respectively). A linear regression line fit to the data for significant relationships ( $p < 0.05$ ) is shown by the solid coloured lines. See Table 3 for linear regression statistics.

Table 3: Statistics corresponding to the ordinary least squares linear regression test between independent variables: mean event air temperature, cumulative event snowfall, and mean event wind speed, and the dependent variable mean event interception efficiency. The test was run separately for three levels of canopy coverage ( $C_c$ ).

SCL					
Dependent Variable	Name	$C_c$	Adjusted $R^2$	p-value	n
Air Temperature (°C)	Sparse	0.73	-0.032	0.519	19
Air Temperature (°C)	Mixed	0.78	0.141	0.033	26
Air Temperature (°C)	Closed	0.82	0.008	0.297	20
Cumulative Snowfall (kg m <sup>-2</sup> )	Sparse	0.73	-0.038	0.568	19
Cumulative Snowfall (kg m <sup>-2</sup> )	Mixed	0.78	0.030	0.197	26
Cumulative Snowfall (kg m <sup>-2</sup> )	Closed	0.82	-0.049	0.732	20
Wind Speed (m/s)	Sparse	0.73	0.114	0.087	19
Wind Speed (m/s)	Mixed	0.78	0.010	0.275	26
Wind Speed (m/s)	Closed	0.82	0.192	0.030	20

285 Fifteen-minute interval measurements of interception efficiency and air temperature shown  
 286 in Figure 6a were not associated, despite significant relationships for the sparse and mixed  
 287 canopies ( $R^2 < 0.03$ ,  $p < 0.05$ ), due to low predictive power (Table 4). The average interception  
 288 efficiency across differing bins of air temperature also does not show any systematic trend  
 289 (Figure 6a). However, a significantly greater median interception efficiency ( $p < 0.05$ ) was  
 290 found for binned measurements with air temperatures below -6 °C compared to those with  
 291 warmer air temperatures using non-parametric Wilcoxon signed rank test.

292 Mean wind speed was weakly associated with interception efficiency for the sparse ( $R^2 = 0.1$ ,  $p$   
 293 > 0.05) and closed ( $R^2 = 0.2$ ,  $p < 0.05$ ), but not for the mixed canopy ( $p > 0.05$ ) (Table 4). The  
 294 binned data show an increasing trend in interception efficiency with increasing wind speed for  
 295 the sparse and closed canopies (Figure 6b). A comparison of interception efficiencies binned for  
 296 low (< 1 m s<sup>-1</sup>) and high (> 1 m s<sup>-1</sup>) wind speeds by the Wilcoxon signed rank test, showed that

297 high wind speeds had significantly higher ( $p < 0.05$ ) median interception efficiencies compared  
298 to the low wind speed bins for the closed and sparse canopy. Conversely, the Wilcoxon test  
299 showed the mixed canopy, which had an opening in the canopy towards the prevailing wind  
300 direction (Figure 2b), had significantly higher ( $p < 0.05$ ) median interception efficiencies for  
301 the low wind speed bins.

302 Interception efficiency showed no association ( $R^2 < 0.05$ ,  $p > 0.2$ ) with the canopy load mea-  
303 sured at the beginning of the 15-minute intervals (Table 4). The binned data show a small  
304 increase in interception efficiency for all three canopies when the snow load is less than  $7 \text{ kg m}^{-2}$   
305 (Figure 6c). Interception efficiency later declined for snow loads greater than  $7 \text{ kg m}^{-2}$  for all  
306 canopies, though this was inconsistent for the mixed canopy. A significantly greater ( $p < 0.05$ )  
307 median interception efficiency was found for canopy snow loads less than  $10 \text{ kg m}^{-2}$  than those  
308 with high initial canopy snow loads ( $> 10 \text{ kg m}^{-2}$ ) using the Wilcoxon rank-test. Additional  
309 statistics from ordinary least squares regression test on the 15-minute interval measurements  
310 are provided in Table 4.

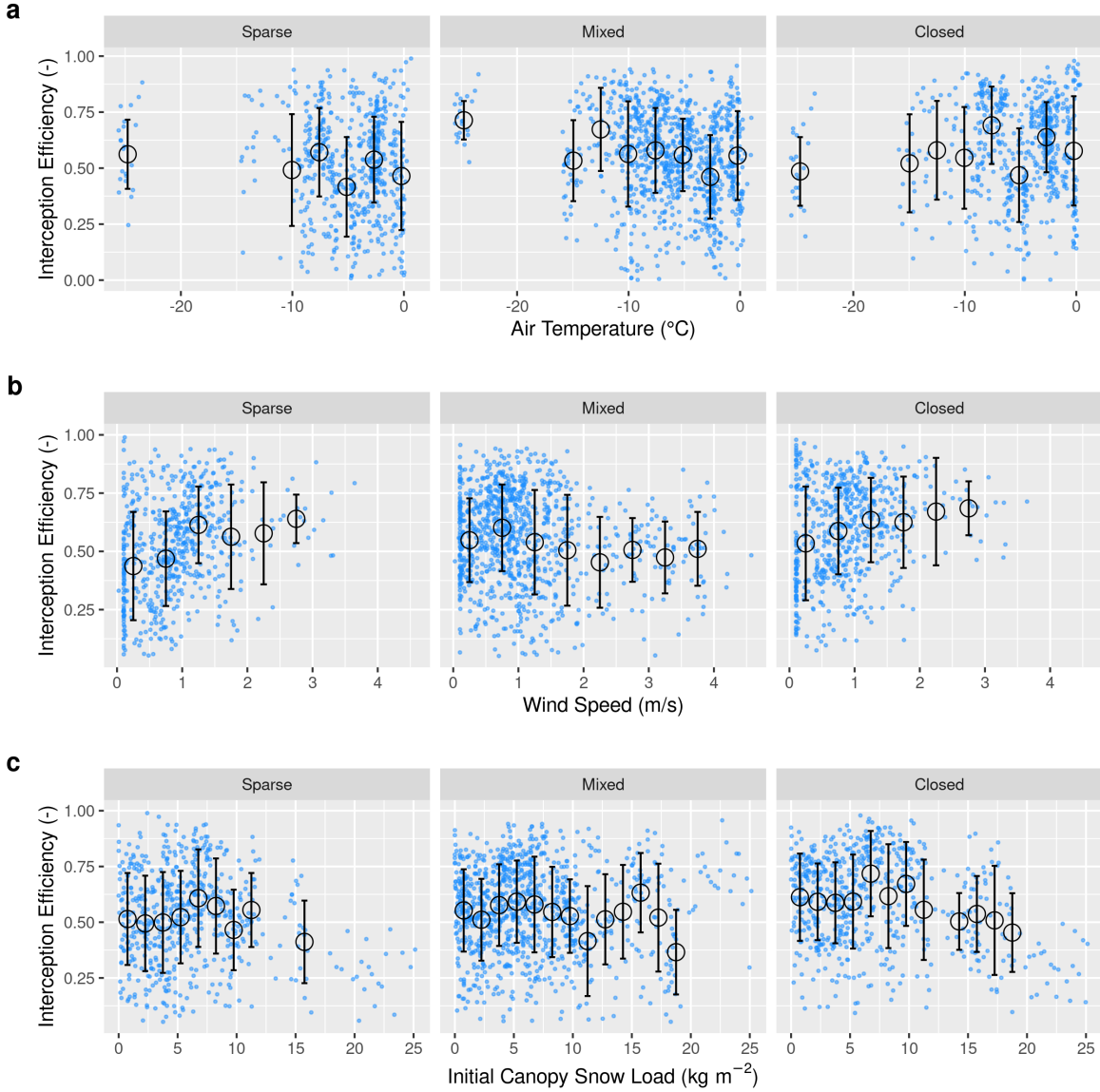


Figure 6: Scatter plots of 15-minute interval measurements (blue dots) and binned data (black open circles with error bars) of mean air temperature, mean wind speed, and initial canopy snow load versus mean snow interception efficiency. Panels show (a) air temperature, (b) wind speed, and (c) initial canopy snow load (the snow load observed at the beginning of the timestep). The black open circles show the mean of each bin and the error bars represent the standard deviations. See Table 4 for linear regression statistics.

Table 4: Statistics corresponding to the ordinary least squares linear regression test between 15-minute interval measurements of independent variables: mean air temperature, mean wind speed, and initial canopy snow load and the dependent variable mean interception efficiency. The test was run separately for three levels of canopy coverage ( $C_c$ ).

Dependent Variable		SCL	$C_c$	Adjusted $R^2$	p-value	n
Air Temperature (°C)	Mixed	0.78	0.032	0.000	985	
Air Temperature (°C)	Closed	0.82	0.004	0.069	618	
Air Temperature (°C)	Sparse	0.73	0.007	0.019	603	
Wind Speed (m/s)	Mixed	0.78	0.017	0.000	985	
Wind Speed (m/s)	Closed	0.82	0.037	0.000	618	
Wind Speed (m/s)	Sparse	0.73	0.089	0.000	603	
Initial Canopy Snow Load (kg m <sup>-2</sup> )	Mixed	0.78	0.000	0.453	972	
Initial Canopy Snow Load (kg m <sup>-2</sup> )	Closed	0.82	0.051	0.000	607	
Initial Canopy Snow Load (kg m <sup>-2</sup> )	Sparse	0.73	0.025	0.000	592	

## 4.2 The influence of forest structure on snow interception

UAV-lidar measurements of throughfall and canopy structure provide insights on how the forest canopy influenced subcanopy snow accumulation during a wind-driven snowfall event between March 13<sup>th</sup> and 14<sup>th</sup> 2023. This event totaled 28.7 kg m<sup>-2</sup> of snowfall at PWL station and was characterized by a transition from low rates of snowfall and air temperatures near 0°C to higher rates of snowfall by late afternoon on March 13<sup>th</sup> coinciding with air temperatures around -2.5 °C. An average wind speed of 1.3 m s<sup>-1</sup> and direction of 188° was observed 4.3 m above the ground at FT Station. Figure 7 shows Cionco's (1965) exponential function for within canopy wind speed was not appropriate for this sparse canopy. The predicted hydrometeor trajectory angles at varying heights, calculated using Equation 4 and the mean observed hydrometeor terminal velocity observed over the event of 0.9 m s<sup>-1</sup> are also shown in Figure 7. An average

322 wind speed of  $1.6 \text{ m s}^{-1}$  and direction of  $188^\circ$  was calculated by integrating the wind speed  
 323 from the surface to the mean canopy height of FT plot. The corresponding trajectory angle  
 324 calculated using Equation 4 from this integrated wind speed was  $61.5^\circ$ .

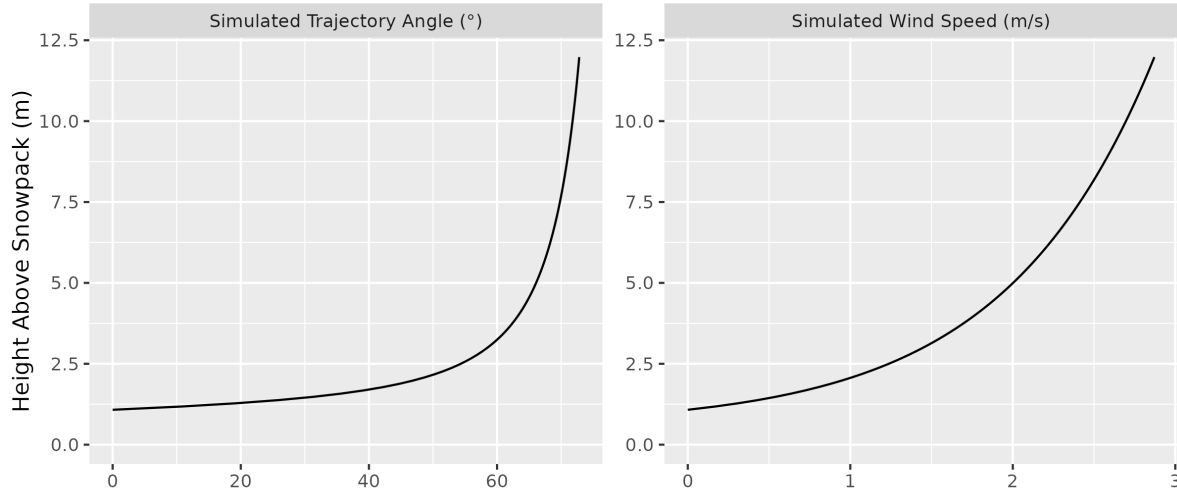


Figure 7: Wind speed profile using roughness length and displacement height parameters derived from anemometers at 2, 3, 4.3, and 13.5 m above ground at FT station over snow free periods and friction velocity estimated over the March 13–14<sup>th</sup> snowfall event.

325 Throughfall depth measured by UAV-lidar was close to the 28 in-situ manual measurements  
 326 with a mean bias of  $-0.001 \text{ m}$  and RMSE of  $0.024 \text{ m}$ . More details on the accuracy of UAV-lidar  
 327 snowdepth measurements are provided in the supporting information section. Figure 8 shows  
 328 the spatial distribution of throughfall and interception efficiency at the PWL and FT forest  
 329 plots. Reduced throughfall and greater interception efficiency was observed on the north (lee)  
 330 side of individual trees, which may be due to non-vertical hydrometeor trajectories caused by  
 331 the steady southerly winds observed over this event. Transparent areas within the forest plots  
 332 in Figure 8 represent grid cells that did not have any lidar ground returns (i.e., under dense  
 333 canopy proximal to tree trunks) or were masked due to disturbance (i.e., walking paths in  
 334 clearings). Visual observations on March 13<sup>th</sup> and 14<sup>th</sup> confirmed non-vertical hydrometeor  
 335 trajectories and increased canopy snow loads were observed on the windward side of individual

<sup>336</sup> trees. This effect is shown in Figure 8 to be more apparent in the PWL forest plot than the  
<sup>337</sup> FT forest plot. This may be attributed to the taller trees and higher canopy coverage of the  
<sup>338</sup> PWL forest plot compared to the FT forest plot, as for the same trajectory angle a taller tree  
<sup>339</sup> will produce a larger downwind footprint.

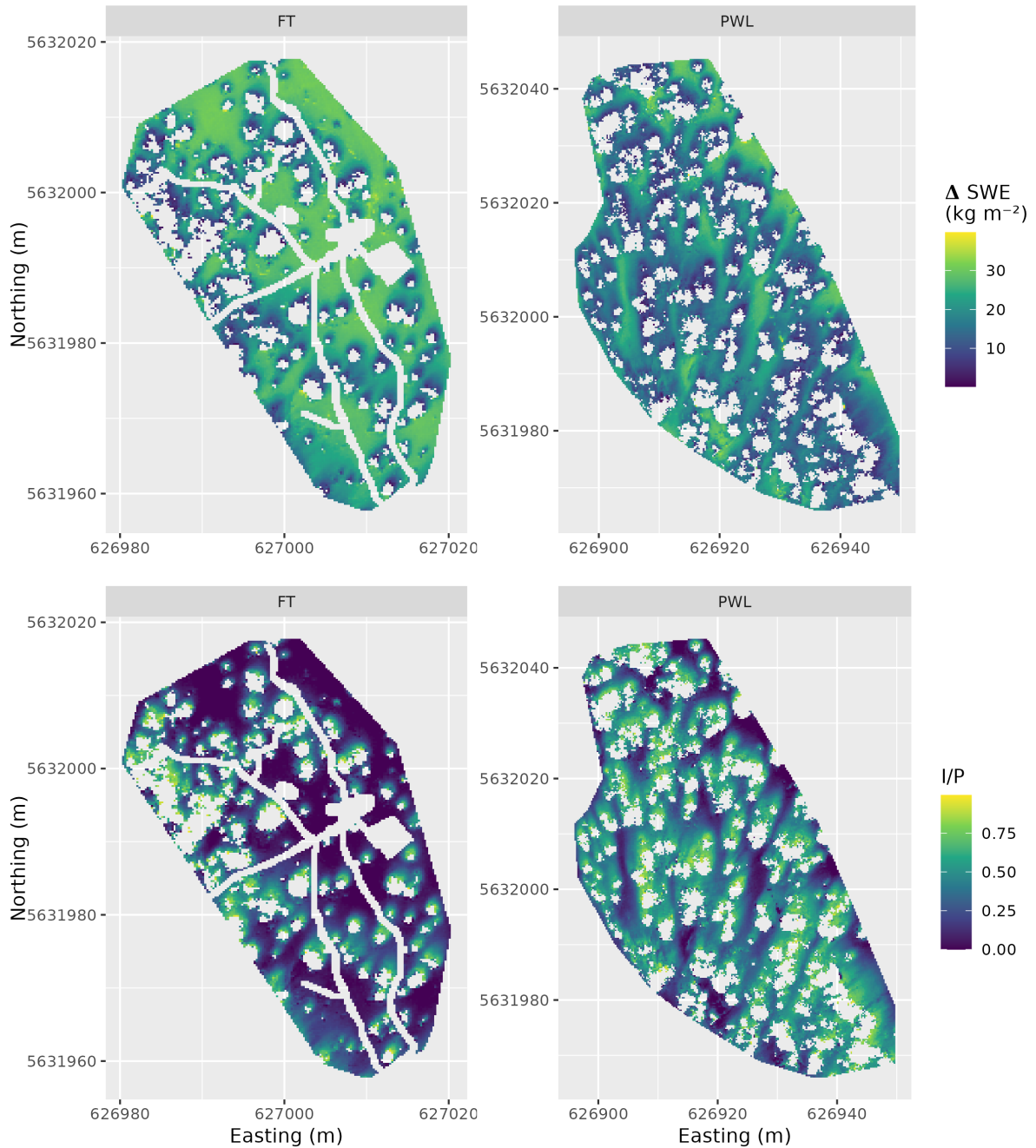


Figure 8: UAV-lidar measurements of the change in snow water equivalent, SWE ( $\text{kg m}^{-2}$ ) and interception efficiency, I/P (-), over the March 13, 2023 24-hour snowfall event for the FT and PWL forest plots at a 0.25 m resolution. See the location of the two forest plots in Figure 1.

Figure 9 shows a strong linear correlation between  $C_p$  and interception efficiency towards the southern portion of the hemisphere, aligning with the average event wind direction. For the PWL forest plot, the upper 97.5<sup>th</sup> percentile of the  $\rho_p$  values shown in Figure 9, were found between azimuth angles of 167°–217°. Similarly, for the FT forest plot, the upper 97.5<sup>th</sup> percentile of  $\rho_p$  was found between azimuth angles of 171°–223°. The zenith angle found to have the highest correlation over this azimuth range was 22° ( $\rho_p = 0.7$ ) and 21° ( $\rho_p = 0.83$ ) for PWL and FT respectively. The high correlation coefficients found for non-vertical zenith angles for both PWL and FT are hypothesized to result from non-vertical hydrometeor trajectories.

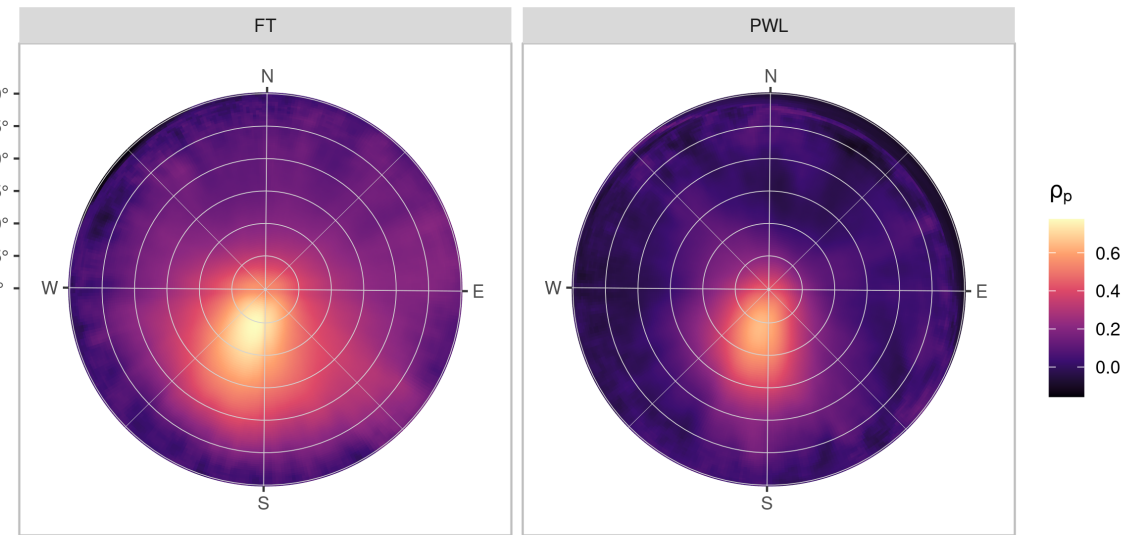


Figure 9: The Pearson Correlation Coefficient between rasters (0.25 m resolution) of interception efficiency and leaf contact area for each grid cell across the study site for each azimuth angles (0°, 1°, ..., 359°) and zenith angles (0°, 1°, ..., 90°) for the FT (left) and PWL (right) forest plots.

The correlation between  $C_p$  and interception efficiency, resampled to a 5 m grid resolution, was higher when  $C_p$  was adjusted for the observed shift in hydrometeor trajectory (Vector Based), compared to the leaf contact angle measured at a zenith angle of 0° (nadir) (Figure 10). The azimuth and zenith angles observed to have the highest  $\rho_p$  in Figure 9 was used to adjust

353 the vector based,  $C_p$  in Figure 10. The stronger association for the vector-based calculation  
 354 suggests that adjusted  $C_p$  is a useful predictor of interception efficiency before ablation. An  
 355 ordinary least squares linear regression forced through the origin was fit to the observed data  
 356 points using the following equation:

$$\frac{I}{P} = C_p(C_c, \theta_h) \cdot \alpha \quad (9)$$

357 where  $\alpha$  is an efficiency constant which determines the fraction of snowflakes that contact the  
 358  $C_p$  elements and are stored in the canopy (i.e., intercepted) before canopy snow unloading or  
 359 ablation processes begin.

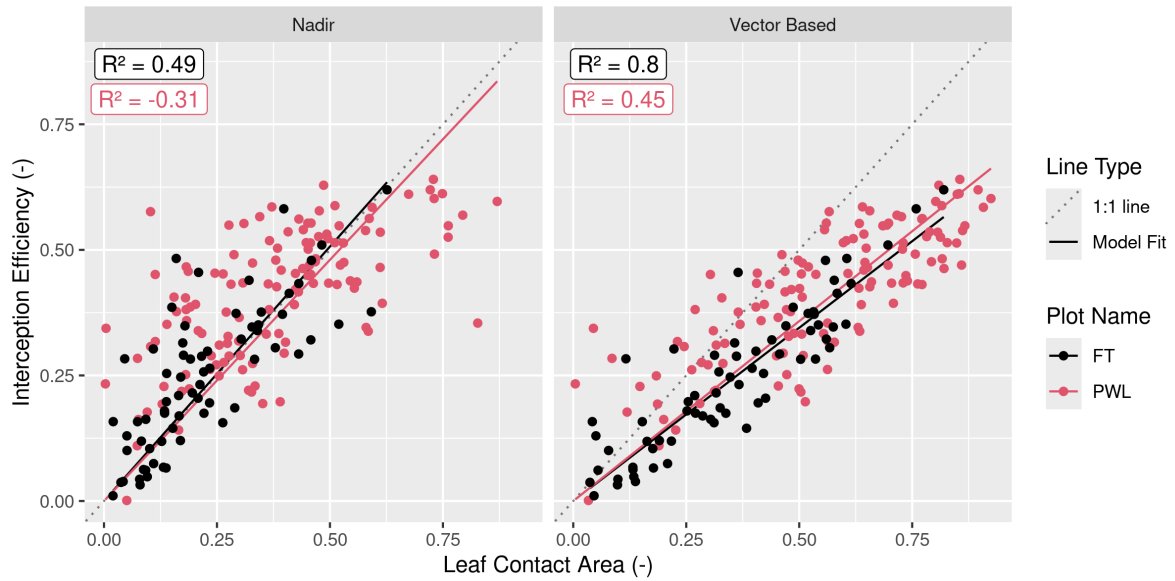


Figure 10: Scatter plots showing the relationship between leaf contact area and interception efficiency rasters resampled to a 5 m grid cell resolution. The left plot (nadir) shows leaf contact area measured from a zenith angle of 0°. The right plot (Vector Based) shows the leaf contact area averaged over rasters with zenith angles (PWL = 22°, FT = 21°) and azimuth angles (PWL = 167°, 178°, ... 217°; FT = 171°, 172°, ... 223°). The solid lines (Model fit) show an ordinary least squares linear regression forced through the origin and fitted to the PWL (red) and FT (black) data and the light grey dotted line shows a 1:1 line. The  $R^2$  values for the four different models are shown in the upper right of each panel calculated following the methods outlined in Kozak & Kozak (1995).

360 For the vector-based model, the relationship between interception efficiency and  $C_p$  results in  
361  $R^2$  values of 0.47 and 0.8 for PWL and FT respectively. The increase in interception efficiency  
362 with  $C_p$  follows a reduced slope compared to the nadir models with  $\alpha$  values of 0.71 and 0.68  
363 for the PWL and FT vector-based models respectively. The reduced slope for the vector-based  
364 models may be due to snowflakes that weaved through and/or bounced off branch elements  
365 in addition to UAV-lidar measurement uncertainty which may have been slightly affected by  
366 unloading and redistribution. These processes would have reduced the fraction of snowfall  
367 that was stored in the canopy. Model error statistics are presented in Table 5 for the nadir  
368 and vector-based models and show the vector-based model provided a better prediction of  
369 interception efficiency. Some of the scatter observed in the nadir model shown in Figure 10  
370 may be explained by grid cells which observed a greater interception efficiency compared to  
371 the corresponding  $C_c$  value and can be attributed to the inability of  $C_c$  to represent the  
372 increase in interception observed within canopy gaps in Figure 8. Conversely, grid cells where  
373 interception efficiency is less than  $C_c$ , may be affected by non-vertical trajectory hydrometeors  
374 making their way underneath the canopy as observed by the reduced interception efficiency  
375 on the windward edges of individual trees in Figure 8. The latter explanation suggests the  
376 non-linear relationship observed for the PWL nadir calculation in Figure 8.

Table 5: Model error statistics provided for predictions of interception efficiency using Equation 9 and for different  $a$  values, as shown in the Model Slope column. Statistics are provided for the PWL and FT forest plots, using leaf contact area canopy metrics adjusted to zenith angles of ( $0^\circ, 1^\circ, \dots 30^\circ$ ) and azimuth angles ( $170^\circ, 171^\circ, \dots 220^\circ$ ) and nadir zenith angle of  $0^\circ$ . The Mean bias is the difference in the model and observed values, MAE is the mean of the absolute error, RMS Error is the root mean squared error,  $R^2$  is the coefficient of determination adjusted using Equation 10 in Kozak & Kozak (1995).

Plot	Canopy	Model Slope	Mean Bias	MAE	RMS Error	
Name	Calculation	(-)	(-)	(-)	(-)	$R^2$
FT	Nadir	0.99	0.022	0.071	0.099	0.51
FT	Vector Based	0.68	0.001	0.047	0.062	0.80
PWL	Nadir	0.95	0.048	0.113	0.146	NA
PWL	Vector Based	0.71	0.019	0.078	0.095	0.47

**377 4.3 The combined influence of trajectory angle and forest structure on  
378 interception**

379 Figure 11 shows that  $C_p$ , measured from VoxRS prior to snowfall on March 13<sup>th</sup>, increases  
380 substantially with simulated hydrometeor trajectory angle and corresponding simulated wind  
381 speed. The standard deviation in VoxRS measured  $C_p$ , illustrated by the shaded area in  
382 Figure 11, exhibits the broad range in values for individual grid cells across each forest plot.  
383 Despite this large scatter, a systematic increase in the mean  $C_p$  across both forest plots results  
384 from a rise in the number of canopy elements for more horizontal angles, when averaged across  
385 each forest plot, over all azimuth angles (see top left panel Figure 11). This results in a large  
386 rise in  $C_p$  over relatively common estimated wind speeds. For example, with a wind speed  
387 of  $1 \text{ m s}^{-1}$  and estimated trajectory angle of  $48^\circ$ ,  $C_p$  would increase by 0.31 and 0.28 for the  
388 PWL and FT forest plots respectively (Figure 11). This is a fractional increase in the plot  $C_p$   
389 from nadir of 0.61 and 0.95 for PWL and FT respectively. The increase in  $C_p$  from  $C_c$ , with  
390 increasing trajectory angle is shown on the bottom row of Figure 11 and exhibits a similar

391 relationship for both forest plots FT and PWL until trajectory angles reach approximately  
392  $60^\circ$ . Beyond  $60^\circ$ , the PWL rate of increase slows as the  $C_p$  approaches 1.0, while the FT plot,  
393 which has lower  $C_c$ , continues to rise until around  $75^\circ$  as a  $C_p$  of 1.0 is approached.  $C_p$  was  
394 also quantified across trajectory angles for both PWL and FT on March 14<sup>th</sup>, post snowfall,  
395 and showed a negligible increase in  $C_p$  compared to  $C_p$  measured on March 13<sup>th</sup> without snow  
396 in the canopy.

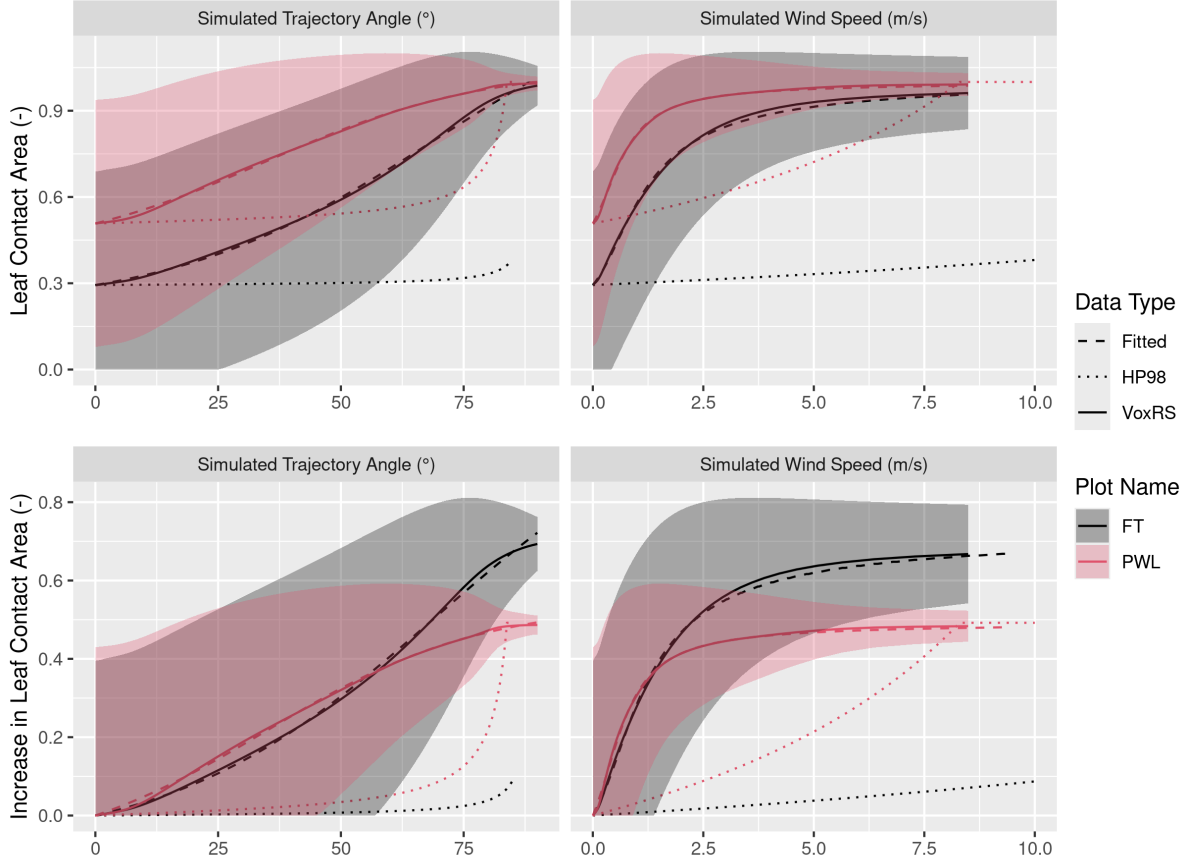


Figure 11: Plots showing the relationship between hydrometeor trajectory angle (left) and wind speed (right) with mean plot-wide snow-leaf contact area,  $C_p$  (top row) and the increase in mean plot-wide  $C_p$ , i.e.,  $C_p - C_c$  (bottom row). The hydrometeor trajectory angle is simulated through VoxRS and is measured as degrees from zenith. Simulated wind speed was calculated as a function of hydrometeor trajectory angle by rearranging Equation 4 and an observed event hydrometeor velocity of 0.9 m s<sup>-1</sup>. The solid lines (VoxRS) represent the mean  $C_p$  (top row) or increase in mean  $C_p$  (bottom row) for a single zenith angle observed from VoxRS across all grid cells for each forest plot and across all azimuth angles. The shaded area represents 1 standard deviation above and below the observed VoxRS mean. The dashed lines (Fitted) represent predictions from Equation 10 (top) and Equation 11 (bottom). The dotted lines (HP98) represent the predictions from Equation 10 in Hedstrom & Pomeroy (1998). A forested downwind distance of 100 m was assumed for the HP98 calculation.

<sup>397</sup> A function is proposed here to calculate plot scale leaf contact area,  $C_p$  (-):

$$C_p = C_c + C_{inc}(\theta_h) \quad (10)$$

398 where,  $C_{inc}$  is the increase in leaf contact area from  $C_c$  which is a function of  $\theta_h$ . To estimate  
 399  $C_{inc}$  a non-linear least squares regression using a logistic function forced through the origin was  
 400 fit to the VoxRS measurements at FT and PWL for simulated hydrometeor trajectory angles  
 401 (see dashed lines in bottom row of Figure 11). A logistic function was selected to model this  
 402 relationship, as its shape reflects the slow increase in observed  $C_p$  at near vertical trajectory  
 403 angles, followed by a rapid increase to represent increase canopy area in the middle and lower  
 404 section of individual trees, and the gradual leveling off as  $C_p$  approaches a value of 1.0. The  
 405 logistic function used to predict  $C_{inc}$  as a function of  $\theta_h$  is:

$$C_{inc} = \left( \frac{C_{inc}^{max}}{1 + e^{\left(\frac{\theta_0 - \theta_h}{k}\right)}} - \frac{C_{inc}^{max}}{1 + e^{\left(\frac{\theta_0}{k}\right)}} \right) \quad (11)$$

406 where  $C_{inc}^{max}$  is the maximum value of  $C_{inc}$ ,  $\theta_0$  is the x-value of the sigmoid midpoint and  $k$  is the  
 407 logistic growth rate or steepness of the curve. The coefficients resulting from the non-linear  
 408 least squares regression fit of Equation 11 to the VoxRS dataset are presented in Table 6.  
 409 Simulated  $C_p$  using Equation 10 is shown in the dashed lines in the top row of Figure 11  
 410 and follows the VoxRS-measured mean  $C_p$  closely. Model error statistics shown in Table 7  
 411 demonstrate that Equation 11 performed well, with a mean bias and RMSE of 0.001 (-) and  
 412 0.0054 (-) respectively for PWL, and -0.0004 (-) and 0.0079 (-) for FT. In contrast, Table 7  
 413 reveals that the Hedstrom & Pomeroy (1998) method produced significantly less accurate  
 414 estimates of  $C_p$ , with a mean bias and RMSE of -0.201 (-) and 0.233 (-) respectively for PWL,  
 415 and -0.260 (-) and 0.324 (-) for FT.

Table 6: Coefficients derived from the non-linear least squares regression fit of Equation 11 to the VoxRS dataset.

Plot Names	$C_{inc}^{max}$	$\theta_0$	$k$
PWL	0.66	34.58	22.14
FT	1.18	69.13	26.98

Table 7: Model error statistics calculated for the prediction of leaf contact area from trajectory angle using Equation 11 (nls) and Equation 10 from Hedstrom & Pomeroy (1998) for the PWL and FT forest plots. Mean bias is the difference in the model and observed values, MAE is the mean of the absolute error, RMS Error is the root mean squared error and  $R^2$  is the coefficient of determination. The units for all metrics are dimensionless. A forested downwind distance of 100 m was used for the HP98 calculation.

Model	Plot Name	Mean Bias (-)	MAE (-)	RMS Error (-)	$R^2$
HP98	FT	-0.26	0.26	0.32	0.72
HP98	PWL	-0.20	0.20	0.23	0.44
nls	FT	0.00	0.01	0.01	1.00
nls	PWL	0.00	0.00	0.01	1.00

#### 416 4.4 Throughfall model performance

417 The performance of Equations 9, 10, and 11 in estimating event throughfall was assessed  
 418 against UAV-lidar measurements of throughfall for the March 13–14<sup>th</sup> snowfall event at the  
 419 plot scale for both FT and PWL. Required values for the model included the event mean  
 420 hydrometeor terminal velocity and event total snowfall which were measured at PWL station,  
 421 and wind speed was taken as one-third the mean canopy height using the wind speed profile in  
 422 Figure 7. Additional model inputs include the mean  $C_c$  for each plot which was measured from  
 423 the VoxRS dataset. An  $\alpha$  value of 0.836 (-) was found through calibration which provided the

<sup>424</sup> best fit between observed and simulated interception efficiency at the plot scale for both FT  
<sup>425</sup> and PWL.

<sup>426</sup> Figure 12 shows the vector-based model, computed using Equation 9 with  $C_p$  adjusted for esti-  
<sup>427</sup> mated hydrometeor trajectory angle, closely matches UAV-lidar measurements of throughfall.  
<sup>428</sup> Observed and modelled values of interception efficiency and  $\Delta SWE_{tf}$  are presented in Table 8  
<sup>429</sup> along with corresponding error statistics. Modelled throughfall from the vector-based model  
<sup>430</sup> was 17 kg m<sup>-2</sup> compared to the measured throughfall of 16.6 kg m<sup>-2</sup> for PWL. For FT, the  
<sup>431</sup> vector-based modelled throughfall was 21.8 kg m<sup>-2</sup>, while the measured values were 22.1 kg  
<sup>432</sup> m<sup>-2</sup>. The vector-based model shows a lower mean bias of -0.3 kg m<sup>-2</sup> for PWL and a negative  
<sup>433</sup> bias of 0.3 kg m<sup>-2</sup> for FT, compared to the larger mean bias of -1.6 kg m<sup>-2</sup> for PWL and -0.8  
<sup>434</sup> kg m<sup>-2</sup> for FT with the nadir-model (calculated using  $C_c$  in place of  $C_p$ ). This resulted in a  
<sup>435</sup> large reduction in the percent error in predicted throughfall, from -9.4% with the nadir-model  
<sup>436</sup> to -1.8% with the vector-based model for PWL. A smaller improvement was observed for FT,  
<sup>437</sup> with the percent error in predicted throughfall declining from -3.6% with the nadir-model to  
<sup>438</sup> -1.4% with the vector-based model.

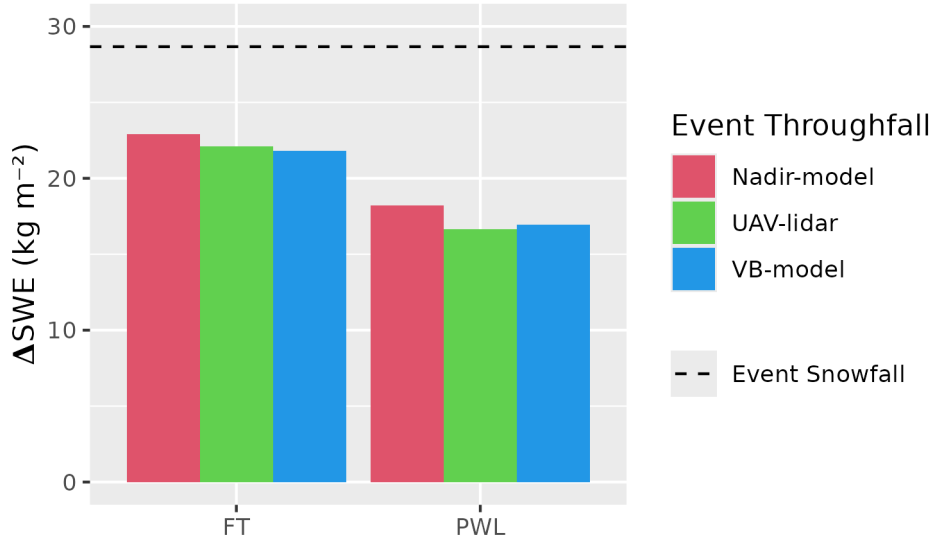


Figure 12: Bar chart comparing the observed and modelled mean change in throughfall ( $\Delta\text{SWE}$ ,  $\text{kg m}^{-2}$ ) over the March 13-14 snowfall event averaged over forest plots FT and PWL. The ‘Nadir-model’ used Equation 9 not adjusted for trajectory angle (i.e.,  $C_c$ ) and the Vector-based ‘VB-model’ which uses Equation 9 with  $C_p$  adjusted for trajectory angle. ‘UAV-lidar’ corresponds to throughfall calculated using Equation 6 incorporating UAV-lidar snow depth and snow density from in-situ snow pits. The black horizontal dashed line shows the accumulated SWE ( $\text{kg m}^{-2}$ ) over the snowfall event to the PWL station open clearing.

Table 8: Model error statistics for model estimates of snow interception efficiency (I/P) and throughfall (TF) compared to measurements of I/P and TF using UAV-lidar averaged over the FT and PWL forest plots. Units for I/P are (-) and TF are ( $\text{kg m}^{-2}$ ). The vector-based model utilized Equation 9 with  $C_p$  adjusted for trajectory angle. The nadir model also utilized Equation 9 but was not adjusted for trajectory angle and thus  $C_c$  was used instead of  $C_p$ . The ‘Obs. Value’ column contains measurements from UAV-lidar while the ‘Mod. Value’ column contains the modelled values. The mean bias was calculated as observed minus modelled and percent error is the percent error between predicted and observed values.

Plot	Model	Value		Obs.	Mod.	Mean	Perc.
Plot	Type	Name	Units	Value	Value	Bias	Error
FT	VB-	I/P	-	0.23	0.24	-0.01	-4.67
	model						
FT	Nadir-	I/P	-	0.23	0.20	0.03	12.10
	model						
FT	VB-	TF	$\text{kg m}^{-2}$	22.12	21.82	0.31	1.38
	model						
FT	Nadir-	TF	$\text{kg m}^{-2}$	22.12	22.91	-0.79	-3.58
	model						
PWL	VB-	I/P	-	0.42	0.41	0.01	2.54
	model						
PWL	Nadir-	I/P	-	0.42	0.37	0.05	12.95
	model						
PWL	VB-	TF	$\text{kg m}^{-2}$	16.64	16.95	-0.31	-1.84
	model						
PWL	Nadir-	TF	$\text{kg m}^{-2}$	16.64	18.20	-1.56	-9.35
	model						

<sup>439</sup> **5 Discussion**

<sup>440</sup> The point scale observations presented in Figure 6 show air temperature had little influence  
<sup>441</sup> on interception efficiency. This differs from existing studies which suggested either a positive  
<sup>442</sup> (Storck et al., 2002) or negative (Hedstrom & Pomeroy, 1998) relationship. A weak relationship,  
<sup>443</sup> that leaves 80–90% of variance unexplained, was observed between initial interception efficiency  
<sup>444</sup> (before unloading) with increasing wind speed at two locations which were sheltered from the  
<sup>445</sup> predominant wind direction (Figure 6b). This is attributed to an associated increase in  $C_p$   
<sup>446</sup> due to non-vertical hydrometeor trajectories. These results are consistent with observations  
<sup>447</sup> by Schmidt & Troendle (1989) who observed a slight increase in snowfall interception with  
<sup>448</sup> increasing wind speeds up to  $6 \text{ m s}^{-1}$  and studies of rainfall interception by Herwitz & Slye  
<sup>449</sup> (1995) and Van Stan et al. (2011).

<sup>450</sup> Compared to the influence of wind speed, interception efficiency showed a smaller sensitivity  
<sup>451</sup> to canopy snow load at the point scale (Figure 5). The slight increase in interception efficiency  
<sup>452</sup> for smaller canopy snow loads and decline for larger canopy snow loads is attributed to the  
<sup>453</sup> influence of canopy snow load on  $C_p$  (Figure 6c). While small, this effect is consistent with  
<sup>454</sup> the theory proposed by Satterlund & Haupt (1967) that interception efficiency increases as  
<sup>455</sup> the canopy fills with snow bridging gaps in the canopy increasing, while later declining due to  
<sup>456</sup> branch bending and decreased canopy coverage. However, the observations shown in Figure 6  
<sup>457</sup> and Figure 3, which minimized ablation processes, differ from those reported by Satterlund  
<sup>458</sup> & Haupt (1967), Schmidt & Pomeroy (1990), and Moeser et al. (2015), as canopy snow load  
<sup>459</sup> increased linearly with snowfalls up to  $45 \text{ kg m}^{-2}$  without approaching a maximum canopy snow  
<sup>460</sup> load. The strong decline in interception efficiency with increasing event snowfall in Satterlund  
<sup>461</sup> & Haupt (1967) and Schmidt & Pomeroy (1990) may have resulted from higher unloading rates  
<sup>462</sup> as branches bent under heavy snow loads, hence mixing ablation and interception processes to  
<sup>463</sup> varying degrees. In contrast, other studies (Calder, 1990; Lundquist et al., 2021; Watanabe &  
<sup>464</sup> Ozeki, 1964) align with the observations in Figure 6 and Figure 3, showing little evidence of  
<sup>465</sup> a reduced interception efficiency with increasing snowfall. The low sensitivity of interception

efficiency with canopy snow load found in this study and others may be attributed to several factors: a reduced inclusion of ablation processes in the interception efficiency measurements, limited influence of canopy snow load on  $C_p$  at this study site, and/or the compensatory effects outlined by Satterlund & Haupt (1967).

Staines & Pomeroy (2023) showed a slight increase in VoxRS measured  $C_p$  between snow-off and snow-on conditions. However, the increase in  $C_p$  resulting from snow load in Staines & Pomeroy (2023) was small compared to the substantial rise in  $C_p$  due to trajectory angle presented in their study and as shown in Figure 11. Both findings from Staines & Pomeroy (2023) corroborate the results reported in this study. Further evidence in support of the relatively small influence of canopy snow load on  $C_p$ , is provided by Lundquist et al. (2021) who reported improved simulation of subcanopy snow accumulation without the use of a maximum canopy snow load, when linked with a comprehensive canopy snow ablation routine. Lehtonen et al. (2016) also note that in northern Finland heavy canopy snow loads have been observed to continue increasing until stem breakage, under conditions favourable for the formation of significant rime-ice accretion and limited ablation, thus reducing  $C_p$ . Models are available to predict the accretion of ice on tree canopies (e.g., Nock et al., 2016) however, further research is required to understand the canopy snow load required to cause stem breakage across different tree species and canopy loads.

These findings on the limited influence of air temperature and canopy snow load on initial interception challenge the theoretical basis of many existing snow interception parameterizations (Hedstrom & Pomeroy, 1998; Moeser et al., 2015; Satterlund & Haupt, 1967; Storck et al., 2002). To address this, a new snow interception parameterization, introduced in Equation 9, is presented which calculates interception efficiency as a function of  $C_p$  and  $\alpha$ . This new parameterization allows for canopy snow loading processes to be isolated from canopy snow ablation processes and is consistent with current rainfall interception theory (Valante et al., 1997). Equation 9 differs only slightly from the original Hedstrom & Pomeroy (1998) parameterization (see Equation 6 in Hedstrom & Pomeroy 1998), in that it does not calculate interception efficiency as a function of canopy snow load and from the Storck et al. (2002)

parameterization who found interception efficiency to be constant. The theoretical basis of the  $\alpha$  parameter in Equation 9 is that the association between  $C_p$  and interception efficiency, as shown in Figure 10, unlike existing rainfall parameterizations (Valante et al., 1997) does not follow a 1:1 line, as falling snow hydrometeors may bounce off the canopy elements. Further research is needed to explore how processes such as the increased cohesion and adhesion of snowfall to the canopy at warm temperatures, as observed by Kobayashi (1987), Pfister & Schneebeli (1999), Storck et al. (2002), as well as hydrometeor velocity, particle size, and shape suggested by (Katsushima et al., 2023), may influence the  $\alpha$  parameter, although these effects were not observed in this study.

Measurements of interception efficiency and canopy structure, as shown in Figure 8, align with the theory proposed by Hedstrom & Pomeroy (1998) which suggests reduced throughfall on the lee side of individual trees for a wind driven snowfall event. However, an existing exponential relationship proposed in Hedstrom & Pomeroy (1998) to scale canopy coverage with wind speed failed to reproduce the observations presented in Figure 11. Instead, plot-wide  $C_{inc}$  was found to increase as logistic function of  $\theta_h$  and  $C_c$ . Significant scatter in VoxRS measured  $C_p$  across the two forest plots, illustrated by the high standard deviation in Figure 11, resulted from directional (azimuth) and spatial differences in canopy structure. This large scatter suggests the observed relationships in Figure 11 are only applicable at the forest stand scale where the sub-metre variability in  $C_p$  averages out. For example, at the point scale, the mixed canopy SCL which is open to the prevailing wind direction (Figure 2), had an increase in throughfall with increasing wind speed (Figure 5 & Figure 6). However, Figure 11 shows that at the plot scale,  $C_p$  rises with increasing  $\theta_h$ , as there is a greater number of grid cells which have more closed canopy at more horizontal angles. Still, Equation 11 would not be applicable to areas that have large continuous gap fractions (e.g., large forested clear cuts) that are many times wider than the mean canopy height. Staines & Pomeroy (2023) have also shown that backflows and large eddies that occur within the canopy can also contribute to mixed responses. Further work is required to refine the relationship proposed in Equation 11 across a range of tree species and densities.

522 It was found that the mean event hydrometeor trajectory angle, required for Equation 11, could  
523 be predicted from Equation 4 using the observed mean hydrometeor fall velocity and the mean  
524 horizontal wind speed selected at one-third of the canopy height above the ground. A wind  
525 speed at one-third the mean canopy height is hypothesized to be important for canopy snow  
526 accumulation as a large fraction of the horizontal cross-sectional area is at this height for most  
527 needleleaf canopies. Katsushima et al. (2023), also proposed the wind speed at one-third the  
528 canopy height for modelling unloading of canopy snow as it corresponds to the centre of gravity  
529 when the horizontal projection of the canopy is assumed to be a triangle. However, there is  
530 uncertainty in the transferability of the canopy height observed here to other environments  
531 due to differing tree structures and tree species. This may include forests with a larger trunk  
532 space or have more of their canopy contact area at higher heights above the ground (i.e., some  
533 deciduous canopies). Moreover, Equation 4 assumes a linear hydrometeor trajectory, and does  
534 not consider non-linear patterns such as wind flow directions around tree elements, turbulent  
535 flow, or differences in wind speed with height.

536 Although the improvement in performance of the vector-based model over the nadir model was  
537 relatively small, the vector-based model is preferred due to its overall lower error compared  
538 to the UAV-lidar measurements and better representation of physical processes. While the  
539 vector-based model acts to increase interception efficiency with wind speed, several studies  
540 have shown that canopy snow ablation increases as a result of wind induced unloading (Bartlett  
541 & Verseghy, 2015; Betts & Ball, 1997; Lumbrago et al., 2022; Roesch et al., 2001; Wheeler,  
542 1987). Thus, representing both the increase in initial interception due to inclined hydrometeor  
543 trajectory angles and the subsequent increase in canopy snow unloading will be important in  
544 subcanopy snow accumulation models.

## 545 **6 Conclusions**

546 New observations of initial snow interception, collected over a wide range of meteorological  
547 conditions and canopy structures indicate that forest structure is the primary factor influencing

548 subcanopy snow accumulation. At the point scale, high-temporal resolution measurements  
549 revealed no evidence of a maximum canopy snow load, even for event snowfalls up to 45 kg  
550  $m^{-2}$ , nor was there any indication of air temperature influencing the cohesion and adhesion of  
551 snowfall to the canopy or branch bending reducing canopy coverage. Instead, wind speed was  
552 found to influence interception efficiency by changing the hydrometeor trajectory angle, which  
553 can lead to a substantial increase in snow-leaf contact area.

554 At the forest plot scale, UAV-lidar measurements of throughfall aligned with the point-scale  
555 observations demonstrating that leaf contact area was the primary factor influencing inter-  
556ception efficiency at a particular site. Leaf contact area, which incorporates changes in the  
557 number of canopy contacts with hydrometeor trajectory angle, proved to be a better predic-  
558 tor of interception efficiency compared to nadir-calculated canopy coverage. When averaged  
559 across each forest plot, leaf contact area was shown to be highly sensitive to trajectory angle,  
560 increasing by 61–95% for trajectory angles associated with a  $1\text{ m s}^{-1}$  wind speed. An existing  
561 theoretical relationship failed to adequately represent the VoxRS-measured increase in leaf  
562 contact area with simulated trajectory angles. As a result, a new relationship is proposed,  
563 which demonstrated good performance at this study site.

564 The weak association between air temperature and canopy snow load with interception effi-  
565 ciency, as presented here and in other recent studies, coupled with the influence of wind speed  
566 on leaf contact area, highlights the need for a new snow interception parameterization. A new  
567 parameterization is proposed that calculates initial interception as a function of snowfall and  
568 leaf contact area. This parameterization is consistent with rainfall interception studies, which  
569 also separate canopy loading and ablation processes, and calculate interception as a function  
570 of canopy coverage. Additionally, a second equation is proposed to estimate leaf contact area  
571 as a function of hydrometeor trajectory angle and nadir canopy coverage. This updated snow  
572 interception parameterization performed well in the subalpine forest studied here. However,  
573 further validation is necessary in a range of climates, forest species, and canopy structures.

<sup>574</sup> **7 Acknowledgments**

<sup>575</sup> We wish to acknowledge financial support from the University of Saskatchewan Dean's Schol-  
<sup>576</sup> arship, Natural Sciences and Engineering Research Council of Canada, Global Water Futures  
<sup>577</sup> Programme, Environment and Climate Change Canada, Alberta Innovates, Canada Founda-  
<sup>578</sup> tion for Innovation, and the Canada Research Chairs Programme. We thank Madison Harasyn,  
<sup>579</sup> Hannah Koslowsky, Kieran Lehan, Lindsey Langs and Fortress Mountain Resort for their help  
<sup>580</sup> in the field. Jacob Staines, Madison Harasyn, Alistair Wallace, and Rob White contributed  
<sup>581</sup> to developing the UAV-lidar processing workflow.

<sup>582</sup> **8 Data Availability**

<sup>583</sup> The data that support the findings in this study are available at <https://doi.org/10.5281/zenodo.14018893>.

584 **References**

- 585 Bartlett, P. A., & Verseghy, D. L. (2015). Modified treatment of intercepted snow improves  
586 the simulated forest albedo in the Canadian Land Surface Scheme. *Hydrological Processes*,  
587 29(14), 3208–3226. <https://doi.org/10.1002/HYP.10431>
- 588 BayesMap Solutions. (2024). *BayesStripAlign*. <https://bayesmap.com/products/bayesstripalign/>
- 589 Betts, A. K., & Ball, J. H. (1997). Albedo over the boreal forest. *Journal of Geophysical  
590 Research: Atmospheres*, 102(D24), 28901–28909. [https://doi.org/https://doi.org/10.1029/96JD03876](https://doi.org/10.1029/96JD03876)
- 591 Calder, I. R. (1990). *Evaporation in the uplands* (p. 148). Wiley.
- 592 Cebulski, A., & Pomeroy, J. W. (2024). The theoretical underpinnings of snow interception  
593 and ablation parameterizations. *Wiley Interdisciplinary Reviews: Water, In Review*.
- 594 Chianucci, F., & Macek, M. (2023). hemispheR: an R package for fisheye canopy image  
595 analysis. *Agricultural and Forest Meteorology*. <https://doi.org/10.1016/j.agrformet.2023.109470>
- 596 Cionco, R. M. (1965). A Mathematical Model for Air Flow in a Vegetative Canopy. *Journal of  
597 Applied Meteorology* (1962), 4(4), 517–522. [https://doi.org/https://doi.org/10.1175/1520-0450\(1965\)004%3C0517:AMMFAF%3E2.0.CO;2](https://doi.org/https://doi.org/10.1175/1520-0450(1965)004%3C0517:AMMFAF%3E2.0.CO;2)
- 598 Ellis, C. R., Pomeroy, J. W., & Link, T. E. (2013). Modeling increases in snowmelt yield and  
599 desynchronization resulting from forest gap-thinning treatments in a northern mountain  
600 headwater basin. *Water Resources Research*, 49(2), 936–949. <https://doi.org/10.1002/wrcr.20089>
- 601 Essery, R., Pomeroy, J. W., Parviainen, J., & Storck, P. (2003). Sublimation of snow from  
602 coniferous forests in a climate model. *Journal of Climate*, 16(11), 1855–1864. [https://doi.org/10.1175/1520-0442\(2003\)016%3C1855:SOSFCF%3E2.0.CO;2](https://doi.org/10.1175/1520-0442(2003)016%3C1855:SOSFCF%3E2.0.CO;2)
- 603 Fryer, B. Y. G. I., Johnson, E. A., Fryer, G. I., & Johnson, E. A. (1988). Reconstructing  
604 Fire Behaviour and Effects in a Subalpine Forest. *The Journal of Applied Ecology*, 25(3),  
605 1063–1072. <https://doi.org/https://doi.org/10.2307/2403766>

- 612 Gelfan, A. N., Pomeroy, J. W., & Kuchment, L. S. (2004). Modeling forest cover influences on  
613 snow accumulation, sublimation, and melt. *Journal of Hydrometeorology*, 5(5), 785–803.  
614 [https://doi.org/10.1175/1525-7541\(2004\)005%3C0785:MFCIOS%3E2.0.CO;2](https://doi.org/10.1175/1525-7541(2004)005%3C0785:MFCIOS%3E2.0.CO;2)
- 615 Golding, D. L., & Swanson, R. H. (1978). Snow accumulation and melt in small forest openings  
616 in Alberta. *Canadian Journal of Forest Research*, 8(4), 380–388. <https://doi.org/https://doi.org/10.1139/x78-057>
- 618 Harder, P., & Pomeroy, J. W. (2013). Estimating precipitation phase using a psychrometric  
619 energy balance method. *Hydrological Processes*, 27(13), 1901–1914. <https://doi.org/https://doi.org/10.1002/hyp.9799>
- 621 Harder, P., Pomeroy, J. W., & Helgason, W. D. (2020). Improving sub-canopy snow depth  
622 mapping with unmanned aerial vehicles: Lidar versus structure-from-motion techniques.  
623 *Cryosphere*, 14(6), 1919–1935. <https://doi.org/10.5194/tc-14-1919-2020>
- 624 Harpold, A. A., Krogh, S. A., Kohler, M., Eckberg, D., Greenberg, J., Sterle, G., & Broxton,  
625 P. D. (2020). Increasing the efficacy of forest thinning for snow using high-resolution  
626 modeling: A proof of concept in the Lake Tahoe Basin, California, USA. *Ecohydrology*,  
627 13(4). <https://doi.org/10.1002/eco.2203>
- 628 Hedstrom, N. R., & Pomeroy, J. W. (1998). Measurements and modelling of snow interception  
629 in the boreal forest. *Hydrological Processes*, 12(10-11), 1611–1625. [https://doi.org/10.1002/\(SICI\)1099-1085\(199808/09\)12:10/11%3C1611::AID-HYP684%3E3.0.CO;2-4](https://doi.org/10.1002/(SICI)1099-1085(199808/09)12:10/11%3C1611::AID-HYP684%3E3.0.CO;2-4)
- 631 Herwitz, S. R., & Slye, R. E. (1995). Three-dimensional modeling of canopy tree interception  
632 of wind-driven rainfall. *Journal of Hydrology*, 168(1-4), 205–226. [https://doi.org/10.1016/0022-1694\(94\)02643-P](https://doi.org/10.1016/0022-1694(94)02643-P)
- 634 Hijmans, R. J. (2024). *terra: Spatial Data Analysis*. <https://cran.r-project.org/package=terra>
- 635 Katsushima, T., Kato, A., Aiura, H., Nanko, K., Suzuki, S., Takeuchi, Y., & Murakami, S.  
636 (2023). Modelling of snow interception on a Japanese cedar canopy based on weighing  
637 tree experiment in a warm winter region. *Hydrological Processes*, 37(6), 1–16. <https://doi.org/10.1002/hyp.14922>
- 639 Kim, E., Gatebe, C., Hall, D., Newlin, J., Misakonis, A., Elder, K., Marshall, H. P., Hiem-  
640 stra, C., Brucker, L., De Marco, E., Crawford, C., Kang, D. H., & Entin, J. (2017).

- 641 NASA's snowex campaign: Observing seasonal snow in a forested environment. *2017*  
642 *IEEE International Geoscience and Remote Sensing Symposium (IGARSS)*, 1388–1390.  
643 <https://doi.org/10.1109/IGARSS.2017.8127222>
- 644 Kobayashi, D. (1987). Snow accumulation on a narrow board. *Cold Regions Science and*  
645 *Technology*, *13*(3), 239–245. [https://doi.org/https://doi.org/10.1016/0165-232X\(87\)90005-X](https://doi.org/10.1016/0165-232X(87)90005-X)
- 646 Kozak, A., & Kozak, R. A. (1995). Notes on regression through the origin. *Forestry Chronicle*,  
647 *71*(3), 326–330. [https://doi.org/https://doi.org/10.5558/tfc71326-3](https://doi.org/10.5558/tfc71326-3)
- 648 Langs, L. E., Petrone, R. M., & Pomeroy, J. W. (2020). A  $\delta^{18}\text{O}$  and  $\delta^2\text{H}$  stable water  
649 isotope analysis of subalpine forest water sources under seasonal and hydrological stress  
650 in the Canadian Rocky Mountains. *Hydrological Processes*, *34*(26), 5642–5658. <https://doi.org/10.1002/hyp.13986>
- 651 LAStools. (2024). *Efficient LiDAR Processing Software (version 240220, academic)*. <http://rapidlasso.com/LAStools>
- 652 Lehtonen, I., Kämärainen, M., Gregow, H., Venäläinen, A., & Peltola, H. (2016). Heavy snow  
653 loads in Finnish forests respond regionally asymmetrically to projected climate change.  
654 *Natural Hazards and Earth System Sciences*, *16*(10), 2259–2271. <https://doi.org/10.5194/nhess-16-2259-2016>
- 655 Lumbrazo, C., Bennett, A., Currier, W. R., Nijssen, B., & Lundquist, J. (2022). Evaluating  
656 Multiple Canopy-Snow Unloading Parameterizations in SUMMA With Time-Lapse  
657 Photography Characterized by Citizen Scientists. *Water Resources Research*, *58*(6), 1–22.  
658 <https://doi.org/10.1029/2021WR030852>
- 659 Lundberg, A., & Hallidin, S. (1994). Evaporation of intercepted snow: Analysis of governing  
660 factors. *Water Resources Research*, *30*(9), 2587–2598. <https://doi.org/10.1029/94WR00873>
- 661 Lundquist, J. D., Dickerson-Lange, S., Gutmann, E., Jonas, T., Lumbrazo, C., & Reynolds, D.  
662 (2021). Snow interception modelling: Isolated observations have led to many land surface  
663 models lacking appropriate temperature sensitivities. *Hydrological Processes*, *35*(7), 1–20.  
664 <https://doi.org/10.1002/hyp.14274>

- 670 MacDonald, J. P. J. (2010). *Unloading of intercepted snow in conifer forests* (Master of  
671 Science August, University of Saskatchewan; pp. 0–93). <http://hdl.handle.net/10388/etd->  
672 09302010-145706
- 673 Moeser, D., Stähli, M., & Jonas, T. (2015). Improved snow interception modeling using  
674 canopy parameters derived from airborne LiDAR data. *Water Resources Research*, 51(7),  
675 5041–5059. <https://doi.org/https://doi.org/10.1002/2014WR016724>
- 676 Musselman, K. N., Pomeroy, J. W., & Link, T. E. (2015). Variability in shortwave irradiance  
677 caused by forest gaps: Measurements, modelling, and implications for snow energetics.  
678 *Agricultural and Forest Meteorology*, 207, 69–82. <https://doi.org/https://doi.org/10.1016/j.agrformet.2015.03.014>
- 680 Nock, C. A., Lecigne, B., Taugourdeau, O., Greene, D. F., Dauzat, J., Delagrange, S.,  
681 & Messier, C. (2016). Linking ice accretion and crown structure: towards a model  
682 of the effect of freezing rain on tree canopies. *Annals of Botany*, 117(7), 1163–1173.  
683 <https://doi.org/https://doi.org/10.1093/aob/mcw059>
- 684 Pfister, R., & Schneebeli, M. (1999). Snow accumulation on boards of different sizes and  
685 shapes. *Hydrological Processes*, 13(14–15), 2345–2355. [https://doi.org/https://doi.org/10.1002/\(SICI\)1099-1085\(199910\)13:14/15%3C2345::AID-HYP873%3E3.0.CO;2-N](https://doi.org/https://doi.org/10.1002/(SICI)1099-1085(199910)13:14/15%3C2345::AID-HYP873%3E3.0.CO;2-N)
- 687 Pomeroy, J. W., Brown, T., Fang, X., Shook, K. R., Pradhananga, D., Armstrong, R., Harder,  
688 P., Marsh, C., Costa, D., Krogh, S. A., Aubry-wake, C., Annand, H., Lawford, P., He,  
689 Z., Kompanizare, M., & Moreno, J. I. L. (2022). The cold regions hydrological modelling  
690 platform for hydrological diagnosis and prediction based on process understanding. *Journal  
691 of Hydrology*, 615(128711), 1–25. <https://doi.org/10.1016/j.jhydrol.2022.128711>
- 692 Pomeroy, J. W., Fang, X., & Ellis, C. R. (2012). Sensitivity of snowmelt hydrology in Marmot  
693 Creek, Alberta, to forest cover disturbance. *Hydrological Processes*, 26(12), 1891–1904.  
694 <https://doi.org/10.1002/hyp.9248>
- 695 Pomeroy, J. W., Marsh, P., & Gray, D. M. (1997). Application of a distributed blowing snow  
696 model to the arctic. *Hydrological Processes*, 11(11), 1451–1464. [https://doi.org/10.1002/\(sici\)1099-1085\(199709\)11:11%3C1451::aid-hyp449%3E3.0.co;2-q](https://doi.org/10.1002/(sici)1099-1085(199709)11:11%3C1451::aid-hyp449%3E3.0.co;2-q)
- 698 Pomeroy, J. W., Parviainen, J., Hedstrom, N., & Gray, D. M. (1998). Coupled modelling of

- 699 forest snow interception and sublimation. *Hydrological Processes*, 12(15), 2317–2337. [https://doi.org/10.1002/\(SICI\)1099-1085\(199812\)12:15%3C2317::AID-HYP799%3E3.0.CO;2-X](https://doi.org/10.1002/(SICI)1099-1085(199812)12:15%3C2317::AID-HYP799%3E3.0.CO;2-X)
- 700
- 701 Pomeroy, J. W., & Schmidt, R. A. (1993). The Use of Fractal Geometry in Modelling Inter-  
702 cepted Snow Accumulation and Sublimation. *Eastern Snow Conference*, 50, 231–239.
- 703 R Core Team. (2024). *R: A Language and Environment for Statistical Computing*. R Foun-  
704 dation for Statistical Computing. <https://www.r-project.org/>
- 705 Rittger, K., Raleigh, M. S., Dozier, J., Hill, A. F., Lutz, J. A., & Painter, T. H. (2020). Canopy  
706 Adjustment and Improved Cloud Detection for Remotely Sensed Snow Cover Mapping.  
707 *Water Resources Research*, 56(6), n/a. <https://doi.org/10.1029/2019WR024914>
- 708 Roesch, A., Wild, M., Gilgen, H., & Ohmura, A. (2001). A new snow cover fraction parame-  
709 terization for the ECHAM4 GCM. *Climate Dynamics*, 17(12), 933–946. <https://doi.org/10.1007/s003820100153>
- 710
- 711 Safa, H., Krogh, S. A., Greenberg, J., Kostadinov, T. S., & Harpold, A. A. (2021). Unraveling  
712 the Controls on Snow Disappearance in Montane Conifer Forests Using Multi-Site Lidar.  
713 *Water Resources Research*, 57(12), 1–20. <https://doi.org/10.1029/2020WR027522>
- 714 Satterlund, D. R., & Haupt, H. F. (1967). Snow catch by Conifer Crowns. *Water Resources  
715 Research*, 3(4), 1035–1039. <https://doi.org/10.1029/WR003i004p01035>
- 716 Schmidt, R. A., & Pomeroy, J. W. (1990). Bending of a conifer branch at subfreezing temper-  
717 atures: implications for snow interception. *Canadian Journal of Forest Research*, 20(8),  
718 1251–1253. <https://doi.org/10.1139/x90-165>
- 719 Schmidt, R. A., & Troendle, C. A. (1989). Snowfall into a forest and clearing. *Journal of  
720 Hydrology*, 110(3-4), 335–348. [https://doi.org/10.1016/0022-1694\(89\)90196-0](https://doi.org/10.1016/0022-1694(89)90196-0)
- 721 Smith, C. D. (2007). Correcting the wind bias in snowfall measurements made with a Geonor  
722 T-200B precipitation gauge and alter wind shield. *87th AMS Annual Meeting*.
- 723 Staines, J., & Pomeroy, J. W. (2023). Influence of forest canopy structure and wind flow  
724 on patterns of sub-canopy snow accumulation in montane needleleaf forests. *Hydrological  
725 Processes*, 37(10), 1–19. <https://doi.org/10.1002/hyp.15005>
- 726 Storck, P., Lettenmaier, D. P., & Bolton, S. M. (2002). Measurement of snow interception  
727 and canopy effects on snow accumulation and melt in a mountainous maritime climate,

- 728 Oregon, United States. *Water Resources Research*, 38(11), 1–16. <https://doi.org/10.1029/2002wr001281>
- 730 Troendle, C. A. (1983). The Potential for Water Yield Augmentation From Forest Management  
731 in the Rocky Mountain Region. *Journal of the American Water Resources Association*,  
732 19(3), 359–373. <https://doi.org/10.1111/j.1752-1688.1983.tb04593.x>
- 733 Valante, F., David, J. S., & Gash, J. H. C. (1997). Modelling interception loss for two sparse  
734 eucalypt and pine forests in central Portugal using reformulated Rutter and Gash analytical  
735 models. *Journal of Hydrology*, 190(1-2), 141–162. [https://doi.org/10.1016/S0022-1694\(96\)03066-1](https://doi.org/10.1016/S0022-1694(96)03066-1)
- 737 Van Stan, J. T., Siegert, C. M., Levia, D. F., & Scheick, C. E. (2011). Effects of wind-  
738 driven rainfall on stemflow generation between codominant tree species with differing crown  
739 characteristics. *Agricultural and Forest Meteorology*, 151(9), 1277–1286. <https://doi.org/10.1016/j.agrformet.2011.05.008>
- 741 Varhola, A., Coops, N. C., Weiler, M., & Moore, R. D. (2010). Forest canopy effects on  
742 snow accumulation and ablation: An integrative review of empirical results. *Journal of  
743 Hydrology*, 392(3-4), 219–233. <https://doi.org/10.1016/j.jhydrol.2010.08.009>
- 744 Vionnet, V., Mortimer, C., Brady, M., Arnal, L., & Brown, R. (2021). Canadian historical  
745 Snow Water Equivalent dataset (CanSWE, 1928–2020). *Earth System Science Data*, 13(9),  
746 4603–4619. <https://doi.org/10.5194/essd-13-4603-2021>
- 747 Watanabe, S., & Ozeki, J. (1964). Study of fallen snow on forest trees (II). Experiment on the  
748 snow crown of the Japanese cedar. *Jap. Govt. Forest Exp. Sta. Bull*, 169, 121–140.
- 749 Wheeler, K. (1987). *Interception and redistribution of snow in a subalpine forest on a storm-  
750 by-storm basis*. Western Snow Conference. <http://sites/westernsnowconference.org/PDFs/1987Wheeler.pdf>